
Very High Resolution Rainfall Patterns measured by TRMM Precipitation Radar: Seasonal and Diurnal Cycles.

Michela Biasutti · Sandra E. Yuter · Casey D. Burleyson · Adam H.

Sobel

Received: date / Accepted: date

ABSTRACT

The TRMM Precipitation Radar is used to construct a high resolution ($0.05^\circ \times 0.05^\circ$) climatology of rainfall over the latitude band extending to about 36° North and South. This study describes climatological patterns of rainfall frequency and intensity at high spatial resolution, with special focus on the seasonal and diurnal cycles in the frequency of rainfall events. We use this Tropics-wide dataset to highlight small-scale precipitation features that are too fine to be captured by the most widely used satellite-based rainfall datasets. The results shed light on the roles of changes in the wind direction, the land-sea thermal contrast, small-scale variations in sea surface temperature, and orography in shaping the seasonal and diurnal cycles of rainfall. In some regions of the tropics, diurnally locked local circulations are largely responsible for sharp gradients in the spatial distribution of seasonal mean precipitation. In other regions, we show that climatological rainfall frequency changes very sharply at coastlines, even though rainfall in these regions is expected to be controlled by relatively large scale weather systems.

M. Biasutti

Lamont-Doherty Earth Observatory, 61 Route 9W. Palisades, NY 10964-8000

Tel.: +1-845-365-8512

Fax: +1 845-365-8736

E-mail: biasutti@ldeo.columbia.edu

S.E. Yuter and C.D. Burleyson

Department of Marine, Earth, and Atmospheric Sciences. North Carolina State University

A.H. Sobel

Department of Applied Physics and Applied Math and Department of Earth and Environmental Sciences. Columbia University

1. Introduction

The Tropical Rainfall Measuring Mission (TRMM) precipitation radar (PR) has provided homogeneous observations over land and ocean over the approximately 36°S-36°N latitudinal band for over a decade now (Kummerow et al. 2000). We have compiled the TRMM PR version 6 observations into a monthly diurnal mean climatology and an annual-mean three-hourly climatology at the native resolution of 0.05°x0.05°(about 5km by 5km); this novel data set describes climatological rainfall characteristics with exquisite spatial detail and relatively uniform coverage, including in regions where surface observations are poor or non-existent. A similar effort was described by Nesbitt and Anders (2009), who discuss some features of the data set including sampling issues. Sobel et al. (2011) have used these data to understand how climatological rainfall rates over small tropical islands depend on island size, showing that precipitation is enhanced over the background oceanic values for islands larger than 315 km², with greater enhancements where lifting over orography is significant. Here we take a bird's view and describe the effect of land/sea contrast and orography over a much broader range of surface features, at both large and small spatial scales, ranging from large islands to continents.

A large body of theoretical and modeling literature has argued over what determines the positions of the marine inter-tropical convergence zone (ITCZ, a very partial list includes Holton et al. 1971; Schneider 1977; Hess et al. 1993; Xie and Philander 1994; Waliser and Somerville 1994; Philander et al. 1996; Biasutti et al. 2005, 2006) and the reach of the monsoons (for example, Rodwell and Hoskins 1996; Joussaume et al. 1999; Chou et al. 2001; Chou and Neelin 2003; Biasutti et al. 2004). In the broadest terms, excess energy input in one or the other hemisphere determines where the centers of net ascent and precipitation larger than local evaporation will be located (Neelin and Held 1987) and—because net precipitation requires moisture convergence—those centers closely correspond to regions of surface wind convergence. At the planetary scale, the positions of rain centers imply the patterns of surface winds as a response to heating. Yet, how rainfall is concentrated or distributed at a range of spatial scales depends on the details of the surface boundary: from patterns of sea surface temperature (SST, see for example the classic paper by Lindzen and Nigam 1987) to land/sea contrast (Webster 1987) and orography (e.g., Prell and Kutzbach 1992; Boos and Kuang 2010). At smaller spatial scales it is local wind patterns that determine the location of rainfall, and interesting seasonal and diurnal patterns emerge; they are the focus of this study.

One principal aim of this paper is to provide a description of a high-resolution rainfall climatology from TRMM PR observations. Although the dataset provides observations at several altitudes, we mostly focus on surface precipitation, which we describe in terms of frequency and intensity of rainfall events. Section 2 offers a description of how the dataset was built and reviews its unique strengths with respects to other TRMM-based products.

In Section 3 we describe the seasonal variations of rainfall frequency and the land/sea contrast in rainfall intensity for selected regions. Most of the large-scale features discussed in this section will not be new to the literature; our contribution is to zoom in on selected regions and draw the reader’s attention to features that are too fine to be captured by the most widely used satellite-based rainfall datasets (e.g. CMAP, GPCP, and TMPA: Xie and Arkin 1996; Adler et al. 2003; Huffman et al. 2007).

The roles of sea and land breezes, mountain and valley breezes, and irregular coastlines in determining local wind circulations and diurnal precipitation distribution are so well known that this topic is covered in introductory meteorology textbooks (e.g. Ahrens 2009, and fig. 16 in Sec. 4). In textbooks, these features are usually described separately. In nature, their effects are often superimposed. Section 4 describes how the interplay of these effects results in substantial differences in the diurnal cycle of rainfall over islands and coastlines in the West Pacific and tropical Americas.

In the Discussion section (Sec. 5) we summarize our results, highlight the role of land/sea contrast in producing some unexpected fine-scale rainfall structures, and propose ways in which this publicly-available, novel dataset might be of use to the climate community.

2. Data

We use the TRMM 2A25 data set, derived from measurements made with the TRMM Precipitation Radar (PR). We use version 6 of the data set, from 1998 to 2007. We first bin the data from each individual swath onto a regular grid with spacing of 0.05 degrees in both longitude and latitude (about a 5km grid). The gridded data are then averaged over the entire record to produce daily-mean monthly climatologies (Sec. 3) and annual-mean diurnal (3-hourly) climatologies (Sec. 4). The nadir point of the TRMM PR swath reaches its highest latitude at 35 deg N/S. The PR swath’s 247 km width means that data are collected up to 123.5 km poleward of 35°latitude which extends the data coverage to just past 36°N/S.

The main variable analyzed in this study is rain frequency: the percentage of observations at a given location for which rain was detected—that is, for which near surface reflectivity was above a threshold of 18 dBZ, corresponding to a rain rate

of 0.4 mm/hr (drizzle and light rain in stratocumulus are not detected by the PR). Data from before and after the satellite boost of August 2001 are treated the same way. The TRMM PR sensor lost some sensitivity at the higher orbit altitude and the resolution of the sensor at the earth's surface went from 18.5km^2 to 25km^2 . The choice of 18 dBZ as a detection threshold is consistent with the post boost minimum sensitivity (Wang and Wolff 2009), and implies that the weakest events ($17 < \text{dBZ} < 18$) that were detected by TRMM pre-boost are not included in the dataset.

Because the TRMM radar takes snapshots, instead of a continuous measurement, the seasonal mean rainfall frequencies are typically less than 15%—even when the gauge measurements indicate that 2 out of 3 days are rainy days. For example, in Darwin, Australia, gauge measurements from the ARM gauge (<http://www.arm.gov/>) over 3 years indicate that rainy days (defined as days with more than 1 mm of accumulation) make up about 55% of the December-through-February rainy season (days with more than 10 mm are about 29%). If we roughly simulate the TRMM sampling by extracting one random hourly value each day from the continuous gauge data and compute the fraction of times that the 0.4mm/h threshold is crossed, we obtain an equivalent TRMM frequency of 12.5% (with a standard deviation of 1.3%). This is in excellent agreement with the frequency that we have computed from actual TRMM PR data (Figure 12) and is consistent with the notion that most rain events are short-lived (Steiner et al. 1995).

We also refer to rain intensity, which is described by the near surface conditional reflectivity, i. e. the mean reflectivity during rain events. Conditional reflectivity in the ice layer (at 6km) is used to further evaluate the intensity of convective events. The 6 km altitude is well above the 0°C level of 4-5 km in the tropics, so these reflectivities are those of precipitation-sized ice. Values less than 28 dBZ are indicative of snow while values larger than 30 dBZ are related to the occurrence of graupel and/or hail. Because hail, in particular, typically occurs within very strong updrafts ($\geq 10 \text{ m/s}$) of spatial extent less than 25 km^2 , beam filling usually reduces the conditional Z in our data set when hail is present. The PR sensitivity loss after the TRMM boost has a minor effect on our conditional intensities: Short and Nakamura (2010) noted an increase of 2%-3% in the probability of reflectivity values between approximately 20-34 dBZ after the orbit boost to a higher altitude.

For our diurnal cycle analysis we use all 120 months of data, aggregated into eight 3-hour blocks, and focus our attention on the region within 25° of the equator. This greatly reduces the susceptibility of the calculated diurnal cycle to the sampling issues highlighted by Hirose and collaborators. Hirose and Nakamura (2005) point out that the samples for an individual month are biased because of uneven diurnal sampling during a month related to the 46 day recurrence period of the TRMM orbit (Negri et al. 2002). These biases are especially noticeable at latitudes higher than 25° (for example, in northern mid-latitudes during August the number of samples is higher in the afternoon than in the morning, Hirose et al. 2008) but they are

reduced closer to the equator. Hirose et al. (2008) determined that the minimum number of samples obtained over 8 years for a 3 hour running mean were adequate to determine the diurnal cycle at 0.2 deg resolution.

The combination of the 5 km x 5 km spatial resolution data from TRMM PR and its coverage from about 36°N to 36°S latitude yields a near-global data set that reveals the spatial distribution of precipitation across the seasonal and diurnal cycles at close to surface-based radar spatial resolutions. This data set provides such information for locations that do not have radar networks or where it is logistically impossible to mount field campaigns. In these regions, sparse rain gauge networks with daily measurements may be present but cannot resolve local circulations (Huffman et al. 2001). The tradeoff is that the TRMM PR temporal sampling is so sparse (less than once every 70 hours near the equator) that data need to be accumulated over multiple years for the persistent spatial patterns to be revealed.

With its combination of high spatial resolution and reliance on a single instrument over ocean and land, this product complements other TRMM-based rainfall products. In particular, TRMM product 3B42 represents a complex blending of data from TRMM and other satellite passive microwave and IR data sets (see trmm.gsfc.nasa.gov/3b42.html and Huffman et al. 2007) and the final rainfall estimates are scaled to match monthly rain gauge totals. It is only by virtue of this data merging that the 3B42 product achieves a spatial resolution of 0.25° x 0.25° and a 3-hourly temporal resolution. Furthermore, the 3B42 data, while useful for many applications, is ill-suited to revealing the role of small local circulations in precipitation spatial distributions since the details of thermally-forced circulations can have scales comparable to single pixels of the 3B42 product. In order to observe the impact of the circulations on precipitation distribution, higher spatial resolutions more typical of ground-based radars are needed.

Additionally, our data set complements field campaign data sets by placing information gleaned from surface-based radars into a larger context. For example, the North American Monsoon Experiment (NAME) took place in northwestern Mexico along and to the west of the Sierra Madre Occidental (Higgins et al. 2006). Observations were obtained from June to September 2004, with a 6-week intensive observation period from 1 July to 15 August that included aircraft missions and more frequent soundings. The details of the diurnal cycle of precipitation reported by Lang et al. (2007), Rowe et al. (2008), Ciesielski and Johnson (2008) and Johnson et al. (2010) among other papers, are based on syntheses of the numerous NAME observations which are not replaceable by TRMM PR data. Yet, TRMM PR both confirms and complements the NAME data sets by filling in information on the precipitation distribution over inaccessible regions of the mountains and showing the increase in precipitation frequency along the Sierra Madre Occidental crest south of the NAME domain.

For comparison to our high spatial resolution data set, we will use the 1998-2007 mean monthly precipitation rates in the GPCP dataset (NASA's Global Precipitation Climatology Project Adler et al. 2003) a global, gridded data set which is based on combined gauge observations, infrared, and microwave satellite estimates and is available on a $2.5^\circ \times 2.5^\circ$ grid.

Surface winds are obtained from QuikSCAT (Graf et al. 1998) over the ocean (for 2000-2007) and from reanalysis over land (ERA Interim, Simmons et al. 2007, for 1998-2007). The ERA winds are simulated at fine (T255, about 0.7°) resolution, but the monthly means used in this study are served by ECMWF at the coarser resolution of 1.5° . Note that, in later figures, we will show land winds with a different scale than that used for ocean winds. In those regions of substantial relief, the wind over the terrain is much weaker than over the adjacent ocean and would not have been visible in the figure had we used the same scaling. Such different wind speeds are physical, and have nothing to do with differences in the data sets (we have confirmed this by looking at reanalysis winds over ocean points as well).

World topography is regredded at 0.05° resolution from the 1-km, quality controlled global Digital Elevation Model (DEM) data from the Global Land One-km Base Elevation (GLOBE) Project (Hastings et al. 1999). As a reference, we show the topography of the regions of interest in Fig. 1.

3. The seasonal cycle

Over the entire tropics, and at both diurnal and seasonal time scales, variations in frequency of rain events explain the lion's share of the variations in rainfall accumulation, with intensity playing a more subtle role. This can be seen in Fig. 2, which compares the annual mean patterns of frequency and intensity of rainfall events in the TRMM PR data to the annual mean rain rates from GPCP over the same period. The correspondence between frequency and rain rates is clear at the large scale, and even in the details: for example in how the East Pacific ITCZ narrows just north of the Galapagos, or in the local maxima on the highlands of Ethiopia and near the coast of Burma (Myanmar). Conversely, intensity is much more uniform; whatever spatial structure it does have—most notably, generally stronger intensity over land than ocean, as noted for example by Zipser et al. (2006)—bears no correspondence to the rain rate structure.

The highest annual mean rain frequencies are in tropical regions with significant coastal or orographic features: near the isthmus of Panama, off the coast of Colombia, and over New Guinea and Borneo (with frequencies near 12%). High frequency is also seen in all of the marine ITCZs, even away from land. The highest rain intensities occur in regions with low frequencies: the central US, Argentina and the western Himalayan indentation. This is consistent with the analysis of

extreme events, the most intense (1% and 0.1%) of Zipser et al. (2006). They found some of the most intense convection in regions with infrequent precipitation where near surface moist flow is capped by dry air aloft. Annual mean rain intensities for central Africa are much higher than over the Amazon, but not quite as high as in the US and Argentina, consistent with the fewer intense events inventoried by Zipser et al. (2006).

Just as they do for the spatial structure of the annual mean rainfall, variations in rain frequency explain the seasonal patterns of rain rates very well. Figures 3, 6, 9, and 12 show the TRMM estimate of seasonal mean rain frequency over Africa, tropical Americas, South Asia, and the West Pacific islands; superimposed on rain frequency is the seasonal mean rain rate calculated from the GPCP data set for the same period. Throughout the tropics, the large scale seasonal movements of the main precipitation centers are captured in the rain frequency field, as are topographic enhancements and rain shadows (these will be shown later in more detail for a few sub-regions).

Over Africa and the Atlantic the frequency field (Fig. 3) captures the well known features of the climatological rain rates: the Atlantic ITCZ is centered north of the equator year round, and only in spring does a weaker secondary ITCZ extend from South America to about 20°W just south of the equator. The convection centers over land follow more or less insolation; maximum rainfall is centered at about 12°N in July, August, September (JAS) and 12°S in January, February and March (JFM). The eastern part of the Sahara desert sees no rain throughout the year, while the western part sees just a couple of rain events per season.

Rain frequency is much higher in the Atlantic marine ITCZ than over Africa, especially during northern summer and fall. The larger oceanic frequency is somewhat compensated by more intense rain over the continent (Fig 4), but the contrast in frequency is dominant and the net effect is larger oceanic rain rates. The main exceptions are in the northern rain band during JAS in the vicinity of orography, in Senegal and Cameron in the west and in Ethiopia in the east, where rain is as frequent as in the ITCZ. High frequencies are also reached in Southern Africa, at about 12°S, during JFM; this too is a region of orographic relief, but—surprisingly—the maximum in rainfall frequency is more zonally uniform than either the local orography or the surface wind is.

Figure 4 shows northern summertime conditional rainfall intensity at the surface and reflectivity in the ice layer at 6km. For reference, the seasonal mean rain rates from GPCP are also shown. In the tropical part of the domain there is an obvious tendency for more intense rainfall over Africa than over the marine ITCZ, but there is not a sharp boundary at the coastline that indicates a direct influence of the lower boundary. Instead, there appear to be a broad correspondence between regions of higher frequency and lower intensity. For example, rainfall over the coast of Guinea and Sierra Leone and over Nigeria

(regions of orographic maxima in frequency) is less intense than over the rest of the continent, and more similar to maritime intensity (but there is no local minimum in intensity over the Ethiopian Highlands, even though rain frequency is high there).

A cleaner separation between land and ocean gridpoints is evident at 6km in the ice layer (Fig 4). Weaker reflectivities, such as in the marine ITCZ, are indicative of snow, while values over the Sahel and Congo indicate the occurrence of graupel or hail, and thus very strong updrafts. As has been noted by numerous authors, the strongest updrafts within convective storms have higher magnitudes over land than ocean. These higher conditional Z values at 6 km altitude imply more common precipitation particle growth by riming over land than ocean. Schumacher et al. (2004) show a stratiform rain fraction over central Africa of 30% compared to 40% in the adjacent ocean which is consistent with this interpretation. We speculate that the lack along the west African coast of a similarly sharp gradient in conditional Z values at the surface indicates that, over the ocean, the lower frequency of riming growth is made up by higher rates of collision/coalescence.

During fall and winter (October, November, December, OND, Fig. 3d and DJF, Fig. 3a and Fig. 5) rainfall is also much more frequent and intense in the Mediterranean sea than along its African coast. There is a remarkably sharp contrast at the coastline between land and ocean values of both frequency of rainfall events and conditional rainfall intensity. This is somewhat unexpected because wintertime rainfall in this region is mostly due to large scale mid-latitude storms and the main winds are northwesterly, blowing from the Mediterranean into Africa (not shown). Yet, despite the large scale of the cyclones, rainfall in the Mediterranean is apparently very sensitive to whether the lower boundary is land or ocean even at very small spatial scale.

The correspondence of larger rain rates with larger rain frequency is also seen in the American sector, both over land and in the East Pacific ITCZ (Fig. 6). The main ITCZ is located at about 10°N for much of the year; it is most intense during northern summer and splits in two weaker ITCZs during northern winter (a remnant of the southern ITCZ is still visible in spring). Over land, precipitation is always more frequent over South America than North America, independent of season. In contrast with the African case, there does not seem to be a systematic difference between the frequency of precipitation over land and ocean, especially over the 10°S-10°N latitude band. Winter precipitation north of 30°N is somewhat more frequent over the Atlantic than over the Southeastern US, but the distinction between land and ocean is not as sharp as it was for the Mediterranean and African region.

The effect of orography is clearly seen alongside the Andes in all seasons and in Central America and southern Mexico in spring and summer. Interesting coastal features also appear at this resolution: for example, during JFM there is a very narrow band of frequent precipitation in the Caribbean, just off the coast of Honduras, Costa Rica, and Panama. Gradients

in sea surface temperature, and consequently latent heat flux, between the colder coastal waters and the warmer Gulf Stream are likely responsible for the alternating bands of weak and strong activity off the coast of Georgia and the Carolinas, especially during spring (April, May, and June, AMJ, Minobe et al. 2008). A local SST minimum is also the cause of a narrow local minimum in JFM precipitation frequency in the Pacific between the ITCZ and South America (a feature that Mapes et al. (2003b) linked to strong wind coming through the orographic gap and cooling local SST), and the minimum off the Caribbean coast of Colombia, especially in AMJ. Land sea contrasts cause Cuba and Hispaniola to experience more rainfall than the surrounding sea during AMJ, but less during OND, and causes Lake Maracaibo, in northeast Venezuela, to experience more rain than the surrounding land all year round, but especially in OND. All these features are tightly locked in position by ocean currents, land-sea contrast and orography, a clear indication that they are robust climatic features.

To gain a better appreciation of the kind of spatial detail visible in this high-resolution climatology, we zoom in on the OND rainfall frequency over the Isthmus of Panama and the northern coast of South America (Fig. 7). On both sides of the land mass the higher rainfall frequencies are found where the surface flow is onshore and perpendicular to the coast, over the Caribbean side of Costa Rica and over the Pacific coast of Colombia. The impact of nearby high mountains is particularly strong west of the Andes, where gravity waves originating over the Andes may enhance convection and aid its propagation off-shore (Mapes et al. 2003a). The effect of the fine scale Andes topography is seen in the banded maxima in the western regions of Colombia, while only a very faint local maximum is visible on the east side of the mountains, where the flow is mostly parallel to the relief. Finally, the maximum in rainfall frequency over Lake Maracaibo seems to be unrelated to features in the large-scale wind, and is discussed in the next section as a consequence of diurnal circulation.

As we did for Africa, we select the northern summer season to describe some broad patterns of intensity in this region (Fig. 8). Here too we notice that the intensity pattern can be interpreted as the superposition of two tendencies: the main one is for intensity to be higher over land than ocean. This is true at large, but also finer scales: contrast, for example, the Caribbean Islands to the adjacent ocean. The other tendency is for land intensity to be weaker over the regions where frequency is high. In northern South America contrast the mean intensity within the 6mm/day rainfall contour to that just outside of it; in Central America contrast the intensity over Nicaragua, versus the Yucatan. Where this latter tendency is dominant, the land/sea contrast in intensity might not be as evident at the coastline (e.g. Nicaragua). Very similar patterns are evident at 6km.

The most prominent feature of the seasonal evolution of rainfall in the Indian sector is, of course, the progression of the monsoon into India and the Bay of Bengal starting in spring and peaking in summer (Fig. 9). As noted by Gadgil (2003),

rainfall in the southern Indian ocean is quite constant over the course of the year, although it is visibly stronger at 15°S during southern summer (JFM) than southern winter (JAS). The effect of the Himalayan massif is visible throughout the year: in winter and fall, it steers midlatitude storms to its south, leaving the plateau with virtually no precipitation; in spring and summer, precipitation occurs on both sides of the Himalayan slope, but it is much stronger to the south, where the monsoon flow impinging on the mountains follows a gradual upslope (Romatschke et al. 2010). The effect of the Western Ghats is limited to spring and summer, when orographic effects on the monsoon flow induce more frequent rainfall both on the western slope and the nearby sea. Alongside the Himalayas, the Ghats, and the Arakan mountains at the border with Burma, the enhancement in rainfall frequency has a narrow spatial scale (Bookhagen and Burbank 2006). Xie et al. (2006) used TRMM PR data at 0.5° resolution to show how these mountain ranges both anchor and broaden the precipitation maxima, yet they puzzle over the indication that the maximum rain rates were displaced from the mountain slopes. At this finer resolution, it is apparent that the maxima in rainfall frequency are not displaced from the slopes (Fig. 10). The most frequent precipitation, by far, is seen on the Burmese coast in the eastern Bay of Bengal during JAS. The coast of Burma is a region of orography, but the large width of the coastal maximum would suggest that other effects, distinct from local orographic enhancement, are at play here. Xie et al. (2006) model the response to the narrow heating associated with precipitation upslope the Arakan mountains and suggest that the mesoscale heating interacts with the large-scale circulation to force a broader rainfall maxima in the Bay of Bengal. Finally, we note the effect of orography in concentrating rainfall frequency in the southeast of Sri Lanka (Fig 9) during AMJ and JAS and, to a lesser degree, in OND. There is a remarkably vast rain shadow to the east of the island during JAS.

The pattern of summertime intensity (Fig. 11) reveals another way in which local orography influences precipitation (Zipser et al. 2006): the most intense precipitation falls at the northwest end of the Himalayas, at the border of India and Pakistan, and along the mountains at the Afghan border, the so-called Western Himalaya indentation. Romatschke et al. (2010) identify these intense events as deep convective cores that originate when moist air flowing from the Arabian sea is capped by continental dry air, and then lifted by the foothills (Medina et al. 2010). Rain events in the indentation are intense but relatively rare: they are maybe a fifth as frequent as those along the eastern portion of the Himalayas or along the Ghats (Fig. 9). Comparing oceanic and continental rainfall intensity in the Indian region does not indicate the expected systematic difference: for example, rainfall off the east coast of India is of very similar intensity or slightly more intense than over the Indian continent and much more intense than over Burma. This is consistent with the distribution of wide convective cores and stratiform rain shown by Romatschke et al. (2010) and with the prevalence of moderate systems with scattered

precipitation that have large extent, slow propagation speed, and long life time in Bangladesh and vicinity (Rafiuddin et al. 2010).

Similar to the other geographic regions, in the Indian region land/sea contrast is clearer in the ice layer: JAS values of conditional Z at 6 km altitude are in general higher over land than ocean. Within the ocean, the Bay of Bengal has higher conditional Z values at 6 km than the equatorial Indian Ocean associated with the convective nature of the monsoon even over water. Leaving aside the Himalayan indentation, there is a gradual increase in conditional Z as one moves southwest from the Ghats to the Himalayas that is more pronounced at 6 km than at the surface. Within the Himalayan indentation, the concentration of conditional Z values greater than 30 dBZ both at the surface and at 6 km altitude indicates storms with very intense updrafts and hail occasionally reaching the surface.

Precipitation in the Maritime Continent (Fig. 12) is frequent throughout the year, and only the continental land masses (the Indochinese peninsula in the Northern Hemisphere and especially Australia in the Southern Hemisphere) experience a true dry season. The relative frequency of land and ocean precipitation is not systematic, but is determined by the complex interplay of land-sea thermal contrast and orographic effects in this region. We do not attempt to describe here all the features of the rainfall field in the West Pacific: we only select a few examples, and complement them by the analysis of the effect of land-sea breezes and mountain-valley breezes in the section concerning the diurnal cycle.

Figure 13 contrast the JFM and JAS patterns of surface winds and precipitation frequency in a region of the West Pacific centered on New Guinea, and including Sulawesi in the northwest corner and New Britain to the east. Southern summer (JFM) is the main rainy season for this region and overall rainfall frequency is larger at this time, while in JAS rainfall retreats to the north. The large scale reversal of winds that accompanies the migration of the monsoon also produces very significant small-scale changes in the rainfall field: rain is far more frequent on the northward (upwind) side of New Britain during JFM and on the southward side in JAS, while a rainshadow develops on the opposite (downwind) side of the island. Around Sulawesi, the pattern of upwind rain and downwind rainshadow is still visible in JAS (around the eastern arms of the island) and during JFM at the northern and southern arms, as well as around the small island of North Maluku, further to the east. But rain is also very frequent over the ocean in between the eastern arms during JFM; here Quicksat shows very weak wind, and the interaction with land is not so easily interpreted in term of the incident flow. The Maoke Mountains of New Guinea are aligned with the wind and have no distinct rain shadow. The elevated heating of the high topography in New Guinea creates bands of frequent precipitation on both slopes throughout the year; this appears to be a true feature, rather than an artifact of the instrumentation, as will be made clear by the analysis of the diurnal cycle in Section 4.

Figure 14 shows OND surface winds and rainfall frequency over Sumatra and Borneo. The large scale northeasterly winds and southeasterly winds converge and turn westerly close to the equator, producing maximum rainfall rates over the eastern side of the Malay Peninsula, but over the western side of Sumatra and Borneo. The rising topography right at the western coast of Sumatra induces a strong maximum over the adjacent ocean, and much less frequent rain on the eastern side of the mountains. Although QuikSCAT winds are parallel to the coast in southern Sumatra, the ERA interim reanalysis over land indicate a small westerly flow there¹, suggesting that the wind is in fact impinging from the ocean onto the mountains even at the southern edge of the island. Over Borneo, the relief is further inland, so the rain shadow effect is muted and rain frequency is uniformly larger here than over Sumatra.

Rainfall intensity in the West Pacific at the time of the Australian monsoon (JFM, Figure 15) shows little spatial structure: there are faint maxima in intensity in Sumatra and Java and off the southern coasts of Sulawesi and New Guinea, but their small scale and unclear relation to local features of land/sea contrast and orography suggest that they might just be noise. In particular, we note the absence of any clear demarcation between land and ocean precipitation in terms of near-surface intensity, either over the Islands or over Australia, but a weak distinction between the two is apparent in the ice layer.

Compared to other geographic regions, the conditional Z at 6 km altitude is generally lower over most of Maritime Continent and there is a smaller difference between conditional Z at 6 km over the larger islands and the surrounding ocean. The implication is that the stronger updrafts tend to occur over land than water but that the difference in updraft strength is smaller than the difference at, say, the African coast. In New Guinea Island and Borneo, locally higher conditional Z values at 6 km altitude tend to occur above mountain slopes rather than at mountain crests. Over Northern Australia, higher reflectivity over land than ocean is somewhat more apparent; this is in contrast with the pattern at the surface, which shows more intense rain in the Gulf of Carpentaria than over the continent.

A global view of 6 km altitude conditional Z indicates that the strongest localized values occur in the Himalayan indentation and the strongest regional values over Africa and North America. While this dataset confirms the well-known tendency for the most intense convection to be over land, it also shows clear regional variations in the typical conditional Z values over land, both at the surface and at 6 km altitude, and a lack of clear demarcation between continental and oceanic Z values along many coasts, especially at the surface. The distinction between a “land regime” and “ocean regime” in rainfall can, in summary, be quite nuanced and blurred—an important finding for satellite-based precipitation estimation, which is based in part on such distinction.

¹ Remember that the scale for wind vectors is different for land points and for ocean points in all the figures, so that land winds, although really much weaker than ocean winds, appear of comparable length.

4. The diurnal cycle

The recognized importance of the diurnal cycle in tropical precipitation distribution was the primary reason that the TRMM satellite was designed to have a precessing rather than sun-synchronous orbit (Simpson et al. 1996). TRMM's temporal sampling is very coarse, especially in the deep tropics, and the choice of high spatial resolution forces us to merge data from all seasons into an accumulated diurnal (3-hourly) climatology in order to get good statistics. Mixing of summertime and wintertime events might be especially problematic in the subtropics, where winter and summer precipitation are of different natures (linked to mid-latitude cyclones or more convective) and the diurnal cycle of rainfall might also be seasonally dependent. Deep in the tropics and in the monsoon regions, we expect that using all seasons will mean that the rainy season is weighted more in the accumulated diurnal cycle, but because rainfall is always associated with convective systems we might hope that any biases would be less problematic. For this reason, and to avoid biases due to sampling issues (Sec 2), this section focuses on tropical regions. In particular, we discuss how diurnally-locked local circulations—sea/land breezes and mountain/valley breezes, interact in shaping the diurnal cycle of rainfall in the islands of the West Pacific and in Meso America, highlighting regions with significant topography near shore and coastlines with pronounced inlets and peninsulas.

Figure 16 provides schematic descriptions of mountain/valley breezes and land/sea breezes. Over coastal land rainfall tends to peak in the early afternoon, but near shore (if nearby mountains are not present) rainfall peaks in the early morning. In regions of elevated topography, precipitation is highest in the early afternoon, but tends to migrate down mountain slopes in the later afternoon toward evening. Combinations of these local circulations can enhance one another. For regions with significant topography near shore, the daytime sea breeze and mountain breeze can combine to produce stronger upslope flow than the mountain breeze would produce independently. Similarly, the land breeze and valley breeze can combine at night to yield stronger offshore flow in regions with coastal mountains. Here, rainfall peaks off shore a bit later than for regions without nearby mountains.

Another factor in enhancing or depressing local circulations is the shape of the coastline and/or mountain ridge. Headlands (land extending seaward) yield localized convergence in conditions of on-shore flow during the day enhancing the sea breeze. At night during off-shore flow, bights (sea extending landward) produce localized convergence that can enhance land-breeze convergence offshore. A similar phenomenon occurs for concave and convex portions of mountain ranges.

The important role of sea/land breeze and mountain/valley breeze circulations on the diurnal cycle was seen in previous work utilizing TRMM PR data including: Mapes et al. (2003b); Nesbitt and Zipser (2003); Barros et al. (2004); Mori et al.

(2004); Bhatt and Nakamura (2005); Hirose and Nakamura (2005); Zhou and Wang (2006); Houze et al. (2007); Cifelli et al. (2008); Hirose et al. (2008); Nesbitt et al. (2008); da Rocha et al. (2009); Romatschke et al. (2010); Takahashi et al. (2010). Many of these studies focused on the time of the largest diurnal peak (e.g. Hirose et al. 2008; Cifelli et al. 2008) or used large regions to resolve the detailed structure of the diurnal cycle (e.g. Nesbitt and Zipser 2003; Cifelli et al. 2008; Romatschke et al. 2010). Our diurnal analysis adds to and refines results from these previous studies by combining information on the duration of the diurnal variation with fine scale geographic variations, especially those related to coastal boundaries and mountain ridges. We also present movies of the diurnal cycle (supplement) which illustrate the migration of convection during the diurnal cycle.

A detailed view of the diurnal cycle of precipitation frequency in the West Pacific is presented in Fig.17 [and supplement movie]. The region of the figure encompasses 6 time zones from 6+ to 12+ UTC. For reference, 00-03 UTC is ~8-11 am local time for longitude 120°E and ~10-13 local time for 150°E. Changes associated with the diurnal cycle will lag in the west compared to the eastern portions of the image. The flattest terrain in the image is associated with the Mekong Delta (10°N 108°E, fig. 1). The island of New Guinea has the sharpest and highest orography in the region, the Maoke Mountains. Near the same latitude, southern Borneo (3°S, 110°E) has relatively more gentle terrain compared to the Muller Mountains in the center and northwest of Borneo. Other large islands of Indonesia, Sumatra, Java, Sulawesi (Celebes), and Timor all have mountain ranges along their lengths (figs. 1, 14 and 13).

A weak diurnal cycle is present over the open ocean. Open ocean areas east of 160°E and west of 100°E have similar spatial patterns and frequency of precipitation overnight from 20 to 08 local (120°E) and a slightly more diffuse pattern and weaker precipitation frequencies during the day. As expected, the largest diurnal variations in precipitation frequency are over land and at the coast.

Mapes and Houze (1993) examined the diurnal cycle of IR detected cold cloud clusters from November through February for the same region. The locations of IR cloud clusters during the day versus at night delineated the larger islands and continental coasts. Our representation, based on PR data, shows how closely the precipitation associated with diurnally-locked local circulations hugs the coastline and mountain ridges (Fig. 18).

Around New Guinea Island, at nighttime the land breeze yields high frequencies of precipitation just offshore (in both the north and south coasts) and the maximum is further amplified by localized convergence in Teluk Sarera (Fig. 18b, annotation A) and in the Gulf of Papua (Fig. 18b, annotation B). During the day, when the breeze is onshore, these same concave regions of coast have lower frequency of precipitation compared to the straighter regions of coastline (Fig. 18a, annotations A and

B). Similar effects are seen in the inlets of Sulawesi. The diurnal behavior of precipitation frequency is similar to what seen for rain rate by Zhou and Wang (2006) and Ichikawa and Yasunari (2008) with coarser resolution data sets.

Precipitation associated with a combination of sea-breeze and mountain breeze circulations is confined to the mountain peaks near midday and then spreads laterally downslope on both north and south sides of the mountain range as afternoon progresses to sunset (Fig. 18a, annotation C). After sunset, there is a local minimum in frequency at the location of the mountain ridge crest as the valley breeze circulation moves the localized convergence away from the peaks and further downslope (Fig. 18a, annotation C). A similar, albeit weaker, local minimum in rainfall frequency is seen in the mountain peak in Borneo at 18-21 UTC. This diurnal pattern of lateral spread of convection associated with the mountain breeze during the afternoon and the valley breeze convection overnight is responsible for the double ridge in diurnal-mean, seasonal-mean precipitation over the Island of New Guinea seen in Section 3. High precipitation frequencies on both sides of the mountains coexist at the same time as land-breeze related precipitation offshore. In the early morning hours before dawn, the valley breeze weakens first, while precipitation offshore continues until after dawn (compare 18-21 UTC to 21 -00 UTC).

The west coast of Sumatra is approximately 40 degree west of the center of New Guinea Island making it 2.6 hours (or about one panel) later. Along the coast run the Barisan Mountains, with elevation over 2000m. The close proximity of the mountains to the shore allows for the land-breeze and valley-breeze circulations to combine and yield very high nighttime precipitation frequencies just offshore. Note that the highest frequencies of land-breeze precipitation offshore occur in the hours before local sunrise (panel g, 21-24 UTC) when the temperature difference between the island and ocean is largest and the land breeze is strongest. In the afternoon (06-09 UTC corresponding to 13-16 local time), the line of high precipitation frequencies along the mountain range is most distinct and there is a thin area of low frequencies along the coast, separating the mountains from the ocean. Similar to the Maoke Mountains in New Guinea, the precipitation associated with the mountain breeze spreads laterally and downslope toward sunset.

In the American sector (Fig. 19 and supplemental movie) we see a similarly rich diurnal cycle. The region depicted in fig. 19 encompasses 2.6 hourly time zones and is centered at 90 W, which corresponds to UTC-6 hours. Similar to the W Pacific, there is only a weak diurnal cycle over the open ocean, but a strong one at the coast. In particular, the concave and convex portions of the coastline of Central America yield localized regions of convergence in different stages of the diurnal cycle. In the Golfo de Panama (Fig. 18cd, annotation D) and in the Caribbean Sea, off the north coast of Panama and the east coast of Costa Rica (Fig. 18cd, annotation E) the concave coastline produces the highest precipitation frequencies near sunrise, when the land-breeze and localized convergence is strongest. The sea-breeze associated precipitation on the

Mosquito Coast (eastern shore of Nicaragua) moves inland over the nearly flat terrain during the afternoon and has additional enhancement related to local convergence over this headland.

As noted by Mapes et al. (2003b) using data at coarser resolution, Venezuela's Lake Maracaibo (Fig. 18cd, annotation F), which is nearly surrounded by land, experiences a very strong diurnal cycle of precipitation frequency and has high frequencies over night (land breeze) and very low frequencies during the day (lake breeze), and diurnal mean frequency greater over the water (Fig 7). The 0.05° resolution data shows how closely the night-time maximum over the lake extends just to the shoreline.

The effect of orography is visible at 15-18 UTC (9-12 local), when individual peaks along the Andes of Columbia and the Guiana Highlands of Venezuela and Brazil experience localized maxima in precipitation frequency associated with mountain breeze circulations (Fig 19).

Further to the north, the magnitude of diurnal variations is less than in the tropics, probably because of both less water vapor and diurnal heating that varies more seasonally. The increase in frequency of precipitation north to south along the peaks of the Sierra Madre of Mexico becomes apparent in the 18-21 UTC panel (11-14 local). Precipitation related to the sea breeze circulation over Cuba peaks at 21-24 UTC (15-18 local). Precipitation frequency sweeps east to west across the Yucatan Peninsula of Mexico during the daylight hours (ref. to supplement movie).

a. Diurnal rainfall intensity

The diurnal cycle of rainfall intensity, shown in terms of conditional radar reflectivity is shown in Figure 20 for both the West Pacific and American regions. Over open ocean there is no distinct diurnal cycle in rainfall intensity. Although open ocean MCS tend to be stronger overnight (Chen et al. 1996; Chen and Houze 1997) they are not frequent enough to bias the conditional Z values in this plot—which are more representative of the nearly ubiquitous tropical oceanic smaller convection (Holder et al. 2008).

Variations in conditional Z over and near land are most apparent in locations with very low precipitation frequency. The concave regions of land have very low frequencies during the afternoon and show up as areas of low conditional Z. Similarly, the low frequencies of precipitation directly over mountain crests in the early morning hours yield lower values of conditional Z in these same regions. Overall, there are slightly higher values of Z over land in the afternoon and slightly lower values of Z over land in the early morning but the delineation between land and ocean is not as distinct as it is in

the precipitation frequency plots. The texture of conditional Z is more variegated in the Americas region compared to the Maritime Continent region.

5. Discussion

We have compiled a seasonal and diurnal climatology of frequency of rainfall events at very high spatial resolution ($0.05^\circ \times 0.05^\circ$) obtained from the precipitation radar aboard TRMM. The choices to include only one instrument and to aggregate the whole data set to retain the native spatial resolution (at the expense of more detailed time information) have produced a climatology that reveals many fine-scale features in the tropical and sub-tropical rainfall. While many of these features have been observed before, they have not been viewed together on a global basis with equal data coverage and quality so that direct quantitative comparison is meaningful.

In both the seasonal and 3-hourly climatological averages, sharp spatial gradients in precipitation accumulation are primarily a result of sharp spatial gradients in precipitation frequency that are locked to surface features, particularly coastlines and orography. This is true even in regimes we think of as dominated by large-scale systems.

At least in the deep tropics (between about 10°S and 10°N), where there is large scale moisture convergence, diurnally locked local circulations are largely responsible for sharp gradients in the spatial distribution of seasonal diurnal mean precipitation frequency. These local circulations persist year-round and can be enhanced or muted by the seasonal large-scale wind field.

The fine details of diurnal circulations are smeared at coarser spatial resolution, but are revealed by this very high spatial resolution climatology, which provides accurate estimates on the reach of land and sea breezes, on the development time of mountain and valley breezes, and especially on how they combine and are modified by wavy coastlines and ridges.

In this work, we have focused on the description of a few of the many salient features in tropical and subtropical climatological rainfall:

As an example of the role of land-sea thermal contrast, we have shown that, in the Caribbean (fig.6), rainfall is more frequent over the islands than over the adjacent ocean during spring and summer, when land is warming faster than the ocean, but less frequent during fall, when the Gulf reaches peak temperatures and cools off slower than land. This see-saw is reminiscent of what happens during the diurnal cycle (fig.19), when peak rainfall moves from the islands (during local afternoon) to the ocean (at night and early morning).

The most striking example of the important interaction between large scale seasonal wind changes and even modest orography is probably given by New Britain (fig. 13), where an intense rain maxima and a rain shadow swap places to the north and south of the island as the global monsoon changes hemisphere.

As an example of how diurnal circulations can combine and be enhanced in bights and headlands, we have shown that thermal and orographic effects are both essential to explain the beautifully rich diurnal cycle of rainfall frequency in the island and along the shore of New Guinea (fig. 17), where rainfall races from the ocean to the coast and up and down the slopes of the mountain ridge dividing the island.

Many more examples were drawn and can be drawn still from this data set, and we hope that our partial selection will inspire other researchers. We envision this dataset to be used by the climate community for studies with many diverse aims, ranging from better understanding of the role of dynamic and thermodynamic controls of rainfall events (in the same vein as Xie et al. 2006; Sobel et al. 2011), to benchmarking of modeling studies (e.g., Lyon et al. 2009; Warner et al. 2003), to bias correction of model output in support of hydrological modeling or climate adaptation for data sparse regions. To this scope, this dataset is made publicly available through a web interface that provides ample capability for extracting and manipulating data (http://kage.ldeo.columbia.edu/SOURCES/.LDEO/.ClimateGroup/.DATASETS/.TRMM_PR).

Acknowledgements This work was supported by NASA grant NNX07AD21G and NSF grants ATM-0544766 and ATM-0908420. Any opinions, findings, and conclusions or recommendations expressed in this material are those of the authors and do not necessarily reflect the views of NASA or NSF.

REFERENCES

- Adler, R. F., et al., 2003: The Version-2 Global Precipitation Climatology Project (GPCP) monthly precipitation analysis (1979-Present). *Journal of Hydrometeorology*, **4**, 1147–1167.
- Ahrens, C., 2009: *Meteorology today: an introduction to weather, climate, and the environment*. 9th ed., Brooks/Cole Pub Co.
- Barros, A., G. Kim, E. Williams, and S. Nesbitt, 2004: Probing orographic controls in the Himalayas during the monsoon using satellite imagery. *Natural Hazards and Earth System Sciences*, **4**, 29–51.

- Bhatt, B. C. and K. Nakamura, 2005: Characteristics of monsoon rainfall around the himalayas revealed by trmm precipitation radar. *Monthly Weather Review*, **133** (1), 149–165, doi:10.1175/MWR-2846.1, URL <http://journals.ametsoc.org/doi/abs/10.1175/MWR-2846.1>, <http://journals.ametsoc.org/doi/pdf/10.1175/MWR-2846.1>.
- Biasutti, M., D. S. Battisti, and E. S. Sarachik, 2004: Mechanisms Controlling the Annual Cycle of Precipitation in the Tropical Atlantic Sector in an Atmospheric GCM. *Journal of Climate*, **17**, 4708–4723.
- Biasutti, M., D. S. Battisti, and E. S. Sarachik, 2005: Terrestrial influence on the annual cycle of the Atlantic ITCZ. *J. Climate*, **18**, 211–228.
- Biasutti, M., A. Sobel, and Y. Kushnir, 2006: AGCM Precipitation Biases in the Tropical Atlantic. *Journal of Climate*, **19** (6), 935–958.
- Bookhagen, B. and D. Burbank, 2006: Topography, relief, and TRMM-derived rainfall variations along the Himalaya. *Geophysical Research Letters*, **33** (8), L08 405.
- Boos, W. and Z. Kuang, 2010: Dominant control of the South Asian monsoon by orographic insulation versus plateau heating. *Nature*, **463** (7278), 218–222.
- Chen, S. and R. Houze, 1997: Diurnal variation and life-cycle of deep convective systems over the tropical Pacific warm pool. *Quarterly Journal of the Royal Meteorological Society*, **123** (538), 357–388.
- Chen, S., R. Houze Jr, and B. Mapes, 1996: Multiscale variability of deep convection in relation to large-scale circulation in TOGA COARE. *Journal of the Atmospheric Sciences*, **53** (10), 1380–1409.
- Chou, C. and J. D. Neelin, 2003: Mechanisms limiting the northward extent of the northern summer convection zones . *J. Climate*, **16**, 406–425.
- Chou, C., J. D. Neelin, and H. Su, 2001: Ocean-atmosphere-land feedbacks in an idealized monsoon. *Q. J. R. Meteorol. Soc.*, **127**, 1869–1891.
- Ciesielski, P. and R. Johnson, 2008: Diurnal cycle of surface flows during 2004 NAME and comparison to model reanalysis. *Journal of Climate*, **21** (15), 3890–3913.
- Cifelli, R., S. Nesbitt, S. Rutledge, W. Petersen, and S. Yuter, 2008: Diurnal Characteristics of Precipitation Features over the Tropical East Pacific: A Comparison of the EPIC and TEPPS Regions. *Journal of Climate*, **21** (16), 4068–4086.
- da Rocha, R., C. Morales, S. Cuadra, and T. Ambrizzi, 2009: Precipitation diurnal cycle and summer climatology assessment over South America: An evaluation of Regional Climate Model version 3 simulations. *Journal of Geophysical Research*,

114 (D10), D10 108.

- Gadgil, S., 2003: The Indian monsoon and its variability. *Annual Review of Earth and Planetary Sciences*, **31** (1), 429–467.
- Graf, J. E., W. Tsi, and L. Jones, 1998: Overview of QuikSCAT mission-a quick deployment of a high resolution, wide swath scanning scatterometer for ocean wind measurement. *Proceedings. IEEE Southeastcon*, p. xiv+416, 314–17, Engineering for a New Era' (Cat. No.98CH36170).
- Hastings, D., et al., 1999: Global Land One-kilometer Base Elevation (GLOBE) Digital Elevation Model, Documentation, Volume 1.0. *Key to Geophysical Records Documentation (KGRD)*, **34**, 1999.
- Hess, P. G., D. S. Battisti, and P. J. Rasch, 1993: Maintenance of the Intertropical Convergence Zones and the Large-Scale Tropical Circulation on a Water-covered Earth. *Journal of Atmospheric Sciences*, **50**, 691–713.
- Hirose, M. and K. Nakamura, 2005: Spatial and diurnal variation of precipitation systems over Asia observed by the TRMM Precipitation Radar. *Journal of Geophysical Research*, **110** (D5), D05 106, doi:doi:10.1029/2004JD004815.
- Hirose, M., R. Oki, S. Shimizu, M. Kachi, and T. Higashiuwatoko, 2008: Finescale diurnal rainfall statistics refined from eight years of TRMM PR data. *Journal of Applied Meteorology and Climatology*, **47** (2), 544–561.
- Holder, C., S. Yuter, A. Sobel, and A. Aiyer, 2008: The Mesoscale Characteristics of Tropical Oceanic Precipitation during Kelvin and Mixed Rossby-Gravity Wave Events. *Monthly Weather Review*, **136** (9), 3446–3464.
- Holton, J. R., J. M. Wallace, and J. M. Young, 1971: On boundary layer dynamics and the ITCZ. *J. Atmos. Sci.*, **28**, 275–280.
- Houze, R., D. Wilton, and B. Smull, 2007: Monsoon convection in the Himalayan region as seen by the TRMM Precipitation Radar. *Quarterly Journal of the Royal Meteorological Society*, **133** (627), 1389–1411.
- Huffman, G., R. Adler, M. Morrissey, D. Bolvin, S. Curtis, R. Joyce, B. McGavock, and J. Susskind, 2001: Global Precipitation at One-Degree Daily Resolution from Multisatellite Observations. *Journal of Hydrometeorology*, **2** (1), 36–50.
- Huffman, G., et al., 2007: The TRMM Multisatellite Precipitation Analysis (TMPA): Quasi-global, multiyear, combined-sensor precipitation estimates at fine scales. *Journal of Hydrometeorology*, **8** (1), 38–55, doi:10.1175/JHM560.1.
- Ichikawa, H. and T. Yasunari, 2008: Intraseasonal variability in diurnal rainfall over New Guinea and the surrounding oceans during austral summer. *Journal of Climate*, **21** (12), 2852–2868.
- Johnson, R., P. Ciesielski, T. L'Ecuyer, and A. Newman, 2010: Diurnal Cycle of Convection during the 2004 North American Monsoon Experiment. *Journal of Climate*, **23** (5), 1060–1078.
- Joussaume, S., et al., 1999: Monsoon changes for 6000 years ago: results of 18 simulations from the Paleoclimate Modeling Intercomparison Project (PMIP). *Geophys. Res. Lett.*, **26**, 859–862.

- Kummerow, C., et al., 2000: The status of the Tropical Rainfall Measuring Mission (TRMM) after two years in orbit. *Journal of Applied Meteorology*, **39** (12), 1965–1982.
- Lang, T., D. Ahijevych, S. Nesbitt, R. Carbone, S. Rutledge, and R. Cifelli, 2007: Radar-observed characteristics of precipitating systems during NAME 2004. *Journal of Climate*, **20** (9), 1713–1733.
- Lindzen, R. S. and S. Nigam, 1987: On the role of sea-surface temperature-gradients in forcing low-level winds and convergence in the tropics. *J. Atmos. Sci.*, **44**, 2418–2436.
- Lyon, B., L. Zubair, V. Ralapanawe, and Z. Yahya, 2009: Finescale evaluation of drought in a tropical setting: Case study in sri lanka. *Journal of Applied Meteorology and Climatology*, **48** (1), 77–88, doi:10.1175/2008JAMC1767.1, URL <http://journals.ametsoc.org/doi/abs/10.1175/2008JAMC1767.1>, <http://journals.ametsoc.org/doi/pdf/10.1175/2008JAMC1767.1>.
- Mapes, B. and R. Houze, 1993: Cloud Clusters and Superclusters over the Oceanic Warm Pool. *Monthly Weather Review*, **121** (5), 1398–1416.
- Mapes, B., T. Warner, and M. Xu, 2003a: Diurnal Patterns of Rainfall in Northwestern South America. Part III: Diurnal Gravity Waves and Nocturnal Convection Offshore. *Monthly Weather Review*, **131** (5), 830–844.
- Mapes, B., T. Warner, M. Xu, and A. Negri, 2003b: Diurnal Patterns of Rainfall in Northwestern South America. Part I: Observations and Context. *Monthly Weather Review*, **131** (5), 799–812.
- Medina, S., R. Houze Jr, A. Kumar, and D. Niyogi, 2010: Summer monsoon convection in the Himalayan region: terrain and land cover effects. *Quarterly Journal of the Royal Meteorological Society*, **136** (648), 593–616.
- Minobe, S., A. Kuwano-Yoshida, N. Komori, S. Xie, and R. Small, 2008: Influence of the Gulf Stream on the troposphere. *Nature*, **452** (7184), 206–209.
- Mori, S., et al., 2004: Diurnal land-sea rainfall peak migration over Sumatra Island, Indonesian maritime continent, observed by TRMM satellite and intensive rawinsonde soundings. *Monthly Weather Review*, **132** (8), 2021–2039.
- Neelin, J. D. and I. M. Held, 1987: Modeling tropical convergence based on the moist static energy budget. *Mon. Wea. Rev.*, **115**, 3–12.
- Negri, A., T. Bell, and L. Xu, 2002: Sampling of the Diurnal Cycle of Precipitation Using TRMM. *Journal of Atmospheric and Oceanic Technology*, **19** (9), 1333–1344.
- Nesbitt, S. and A. Anders, 2009: Very high resolution precipitation climatologies from the Tropical Rainfall Measuring Mission precipitation radar. *Geophysical Research Letters*, **36** (15), L15 815, doi:doi:10.1029/2009GL038026.

- Nesbitt, S., D. Gochis, and T. Lang, 2008: The diurnal cycle of clouds and precipitation along the Sierra Madre Occidental observed during NAME-2004: Implications for warm season precipitation estimation in complex terrain. *Journal of Hydrometeorology*, **9** (4), 728–743.
- Nesbitt, S. and E. Zipser, 2003: The Diurnal Cycle of Rainfall and Convective Intensity according to Three Years of TRMM Measurements. *Journal of Climate*, **16**, 1456–1475.
- Philander, S. G. H., D. Gu, D. Halpern, G. Lambert, N.-C. Lau, T. Li, , and R. Pacanowski, 1996: Why the ITCZ is mostly north of the equator. *J. Climate*, **9**, 2958–2971.
- Prell, W. and J. Kutzbach, 1992: Sensitivity of the Indian monsoon to forcing parameters and implications for its evolution. *Nature*, **360** (6405), 647–652.
- Rafiuddin, M., H. Uyeda, and M. Islam, 2010: Characteristics of monsoon precipitation systems in and around Bangladesh. *International Journal of Climatology*, **30** (7), 1042–1055.
- Rodwell, M. J. and B. J. Hoskins, 1996: Monsoons and the dynamics of deserts. *Q. J. R. Meteorol. Soc.*, **122**, 1385–1404.
- Romatschke, U., S. Medina, and R. Houze Jr, 2010: Regional, seasonal, and diurnal variations of extreme convection in the South Asian Region. *Journal of Climate*, **23** (2), 419–439.
- Rowe, A., S. Rutledge, T. Lang, P. Ciesielski, and S. Saleeby, 2008: Elevation-dependent trends in precipitation observed during NAME. *Monthly Weather Review*, **136** (12), 4962–4979.
- Schneider, E. K., 1977: Axially symmetric steady-state models of the basic state for instability and climate studies. part ii. nonlinear calculations. *Journal of the Atmospheric Sciences*, **34** (2), 280–296, doi:{10.1175/1520-0469(1977)034<0280:ASSSMO>2.0.CO;2}.
- Short, D. A. and K. Nakamura, 2010: Effect of trmm orbit boost on radar reflectivity distributions. *Journal of Atmospheric and Oceanic Technology*, **27** (7), 1247–1254, doi:10.1175/2010JTECHA1426.1, URL <http://journals.ametsoc.org/doi/abs/10.1175/2010JTECHA1426.1>, <http://journals.ametsoc.org/doi/pdf/10.1175/2010JTECHA1426.1>.
- Simmons, A., S. Uppala, D. Dee, and S. Kobayashi, 2007: ERA-Interim: New ECMWF reanalysis products from 1989 onwards. *ECMWF Newsletter*, **110**, 25–35.
- Simpson, J., C. Kummerow, W. Tao, and R. Adler, 1996: On the tropical rainfall measuring mission (TRMM). *Meteorology and Atmospheric physics*, **60** (1), 19–36.

Sobel, A. H., C. Burleyson, and S. E. Yuter, 2011: Rain on small tropical islands. *Journal of Geophysical Research-Atmospheres*, in review.

Steiner, M., R. Houze Jr, and S. Yuter, 1995: Climatological characterization of three-dimensional storm structure from operational radar and rain gauge data. *Journal of Applied Meteorology*, **34** (9), 1978–2007.

Takahashi, H., H. Fujinami, T. Yasunari, and J. Matsumoto, 2010: Diurnal rainfall pattern observed by Tropical Rainfall Measuring Mission Precipitation Radar (TRMM-PR) around the Indochina peninsula. *Journal of Geophysical Research*, **115** (D7), D07 109.

Waliser, D. E. and R. Somerville, 1994: Preferred latitudes of the intertropical convergence zone. *J. Atmos. Sci.*, **51**, 1619–1639.

Wang, J. and D. Wolff, 2009: Comparisons of Reflectivities from the TRMM Precipitation Radar and Ground-Based Radars. *Journal of Atmospheric and Oceanic Technology*, **26** (5), 857–875.

Warner, T., B. Mapes, and M. Xu, 2003: Diurnal patterns of rainfall in northwestern South America. Part II: Model simulations. *Monthly Weather Review*, **131** (5), 813–829.

Webster, P. J., 1987: *Monsoons*, chap. The Elementary Monsoon, 3–32. J. Wiley Co.

Xie, P. and P. A. Arkin, 1996: Analyses of global monthly precipitation using gauge observations, satellite estimates, and numerical model predictions. *J. Climate*, **9**, 840–858.

Xie, S., H. Xu, N. Saji, Y. Wang, and W. Liu, 2006: Role of Narrow Mountains in Large-Scale Organization of Asian Monsoon Convection*. *Journal of Climate*, **19** (14), 3420–3429.

Xie, S. P. and S. G. H. Philander, 1994: A coupled ocean-atmosphere model of relevance to the ITCZ in the eastern Pacific. *Tellus*, **46A**, 340–350.

Zhou, L. and Y. Wang, 2006: Tropical Rainfall Measuring Mission observation and regional model study of precipitation diurnal cycle in the New Guinean region. *Journal of Geophysical Research*, **111** (D17), D17 104.

Zipser, E., C. Liu, D. Cecil, S. Nesbitt, and D. Yorty, 2006: Where are the most intense thunderstorms on Earth? *Bulletin of the American Meteorological Society*, **87** (8), 1057–1071.

List of Figures

- 1 Topography (in meters) at 0.5° resolution in the regions of interest. 26
- 2 Top: Annual mean frequency of rain events (percentage, shaded) and rain rates in the GPCP data (contours, starting at 3mm/day, contour interval is 3mm/day). Bottom: annual mean conditional intensity expressed as mean surface reflectivity (dBZ) during rain events (shaded) and rain rates (as above). 27
- 3 Seasonal mean rain frequency in the TRMM PR data (shaded) and rain rates in the GPCP dataset (white contours, the contour interval is 3mm/day, starting at 3mm/day). 28
- 4 JAS seasonal mean conditional reflectivity (dBZ) at surface (left) and at 6km (right) in the TRMM PR data (shaded) and rain rates in the GPCP dataset (left, white contours, the contour interval is 6mm/day, starting at 6mm/day). 29
- 5 Rain frequency (top) and intensity (bottom) in the southern Mediterranean sea and North African coast during JFM. 30
- 6 Seasonal mean rain frequency in the TRMM PR data (shaded) and rain rates in the GPCP dataset (white contours, the contour interval is 3mm/day, starting at 3mm/day). 31
- 7 (top) Topography and surface winds. Ocean surface winds are taken from Quikscat and are plotted in black every other gridpoint (i.e., at 1° resolution). Land winds are taken from the Interim ERA reanalysis and are plotted in white at 2.5° resolution. For clarity, wind over land is plotted with a scale 8 times as large as that used for ocean winds (that is, a wind vector will appear 8 times as large over land, for the same wind speed). (bottom) Rain frequency in the TRMM PR data. The light black contour indicates orography above 1000m. 32
- 8 JAS seasonal mean conditional reflectivity (dBZ) at surface (left) and at 6km (right) in the TRMM PR data (shaded) and rain rates in the GPCP dataset (left, white contours, the contour interval is 6mm/day, starting at 6mm/day). 33
- 9 Seasonal mean rain frequency in the TRMM PR data (shaded) and rain rates in the GPCP dataset (white contours, the contour interval is 3mm/day, starting at 3mm/day). 34
- 10 Summertime rain frequency in the TRMM PR data along the (left) Ghats and the (right) Arakan mountains. The black (left) or white (right) contours indicate the coast and orography above 1000m. 35
- 11 JAS seasonal mean conditional reflectivity (dBZ) at surface (left) and at 6km (right) in the TRMM PR data (shaded) and rain rates in the GPCP dataset (left, white contours, the contour interval is 6mm/day, starting at 6mm/day). 36
- 12 Seasonal mean rain frequency in the TRMM PR data (shaded) and rain rates in the GPCP dataset (white contours, the contour interval is 3mm/day, starting at 3mm/day). 37

- 13 (left) Topography and surface winds. Ocean surface winds are taken from Quicksat and are plotted in black every other gridpoint
 (i.e., at 1° resolution). Land winds are taken from the Interim ERA reanalysis and are plotted in white at 2.5° resolution. For clarity,
 wind over land is plotted with a scale 4 times as large as that used for ocean winds (that is, a wind vector will appear 4 times
 as large over land, for the same wind speed). (right) Rain frequency in the TRMM PR data. The light black contour indicates
 orography above 1000m. 38
- 14 As in fig.13. 39
- 15 JFM seasonal mean conditional reflectivity (dBZ) at surface (left) and at 6km (right) in the TRMM PR data (shaded) and rain
 rates in the GPCP dataset (left, white contours, the contour interval is 6mm/day, starting at 6mm/day). 40
- 16 Schematic explanation of the basic mechanism for sea breeze (top left and center) and land breeze (middle left and center) and for
 valley (top right) and mountain (middle right) breeze. The bottom panels depict the way in which bights and headlands influence
 land/sea breezes. Similar effects are a consequence of curves in the mountain ranges. 41
- 17 Diurnal cycle of rainfall frequency in 3-hourly increments for the West Pacific region. The left panels are for daytime, the right
 panels are for nighttime. 42
- 18 Late afternoon (left) and pre-dawn (right) rainfall frequency over New Guinea Island (top) and the Panama Isthmus (bottom). 43
- 19 Diurnal cycle of rainfall frequency in 3-hourly increments for the Middle America region. The left panels are for daytime, the
 right panels are for nighttime. 44
- 20 Conditional rainfall intensities for hours near sunset (left) and near dawn (right) for the West Pacific (top) and the Middle America
 (bottom) regions. 45

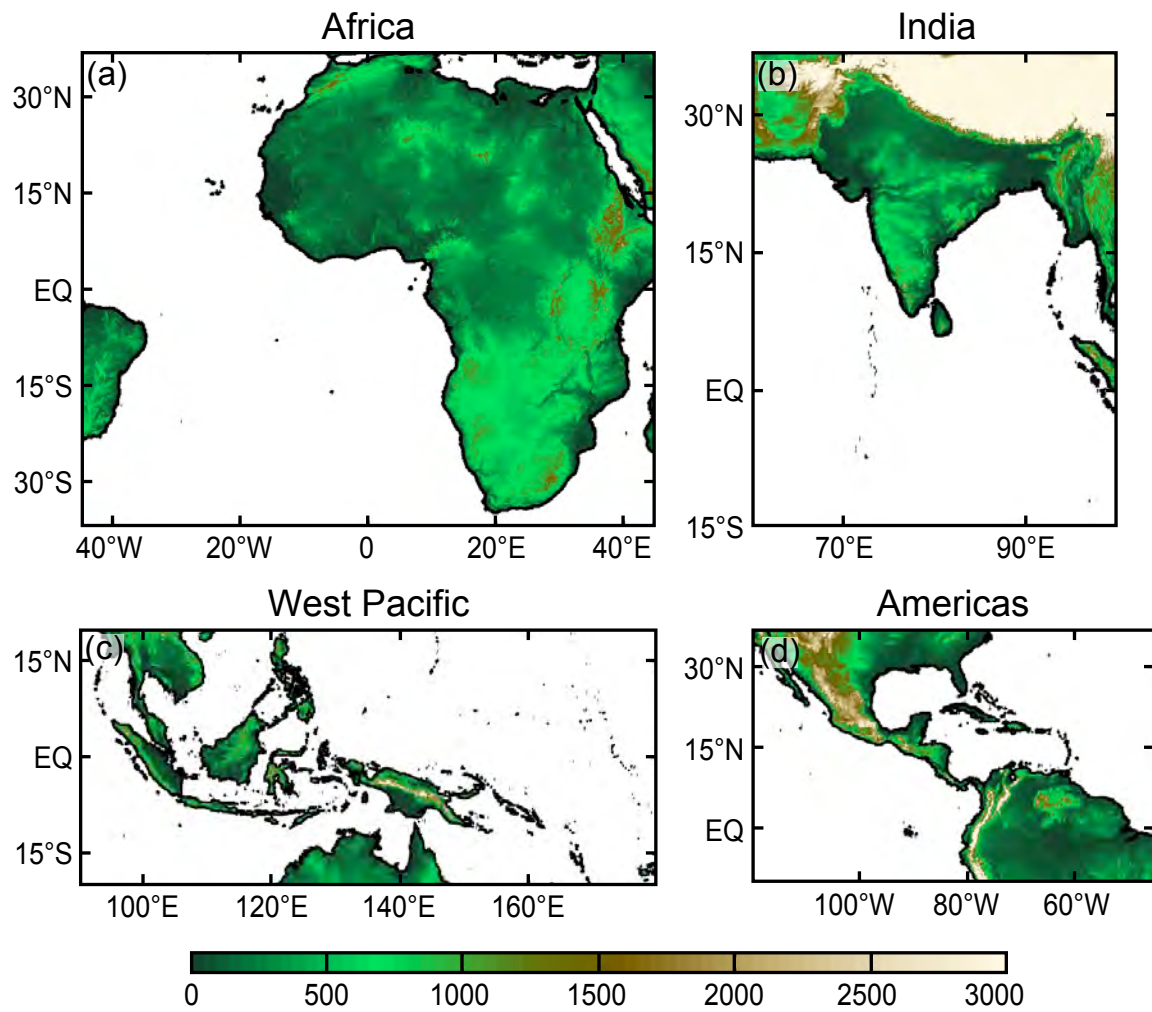


FIG. 1. Topography (in meters) at 0.5° resolution in the regions of interest.

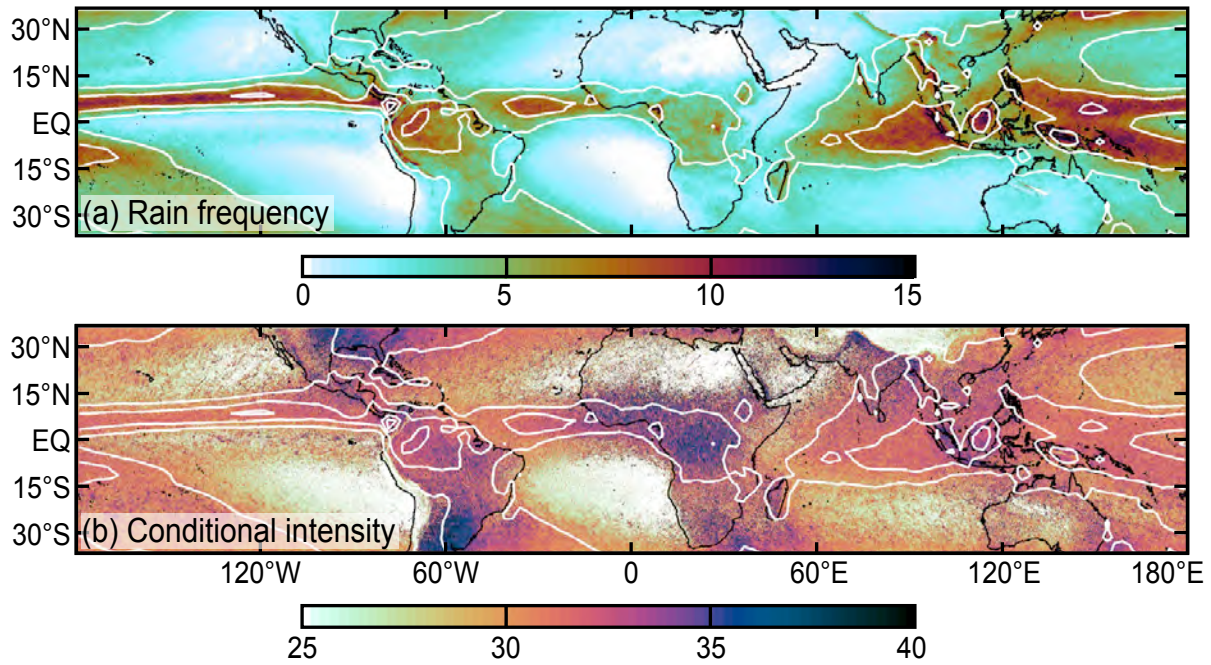


FIG. 2. Top: Annual mean frequency of rain events (percentage, shaded) and rain rates in the GPCP data (contours, starting at 3mm/day, contour interval is 3mm/day). Bottom: annual mean conditional intensity expressed as mean surface reflectivity (dBZ) during rain events (shaded) and rain rates (as above).

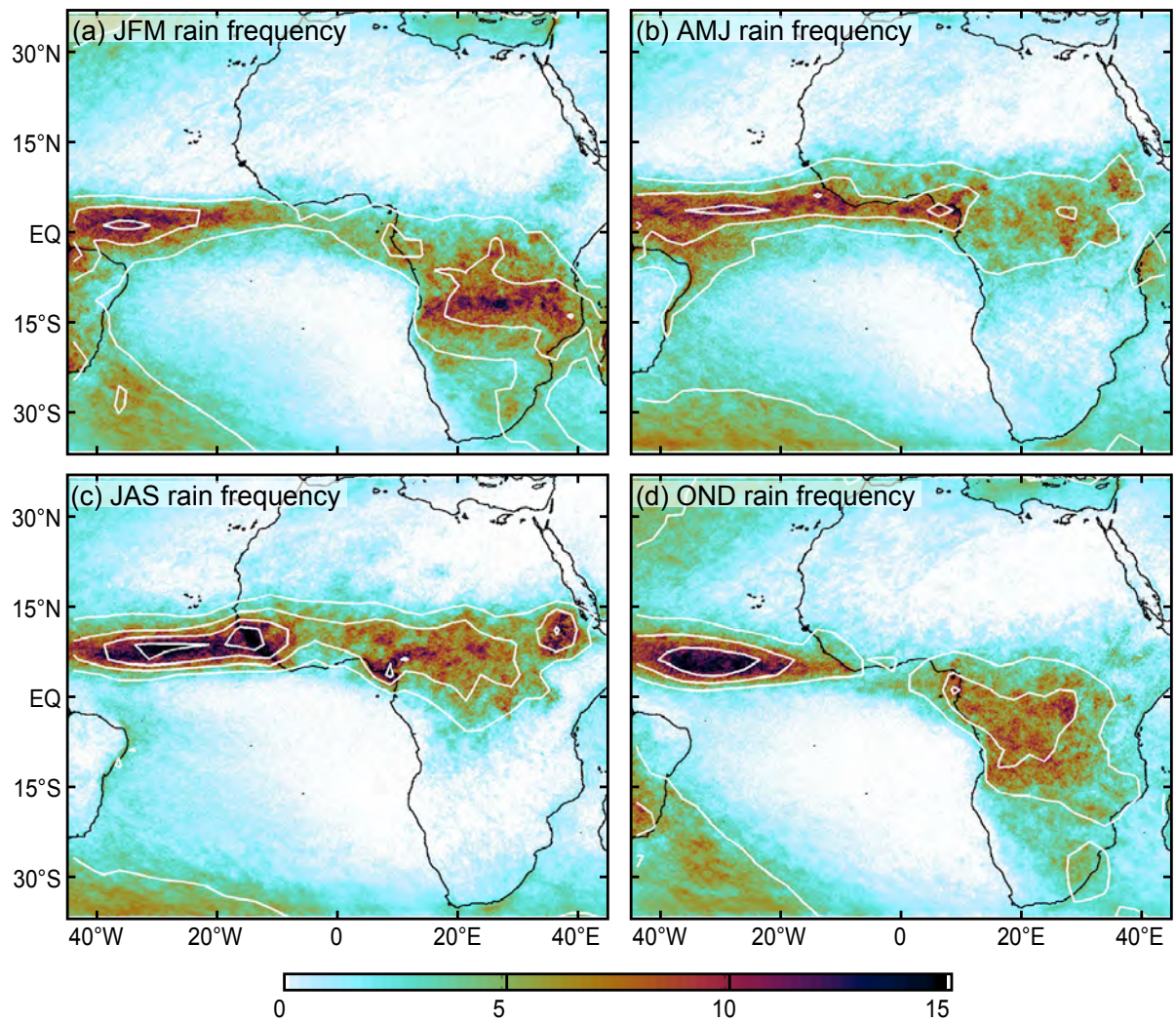


FIG. 3. Seasonal mean rain frequency in the TRMM PR data (shaded) and rain rates in the GPCP dataset (white contours, the contour interval is 3mm/day, starting at 3mm/day).

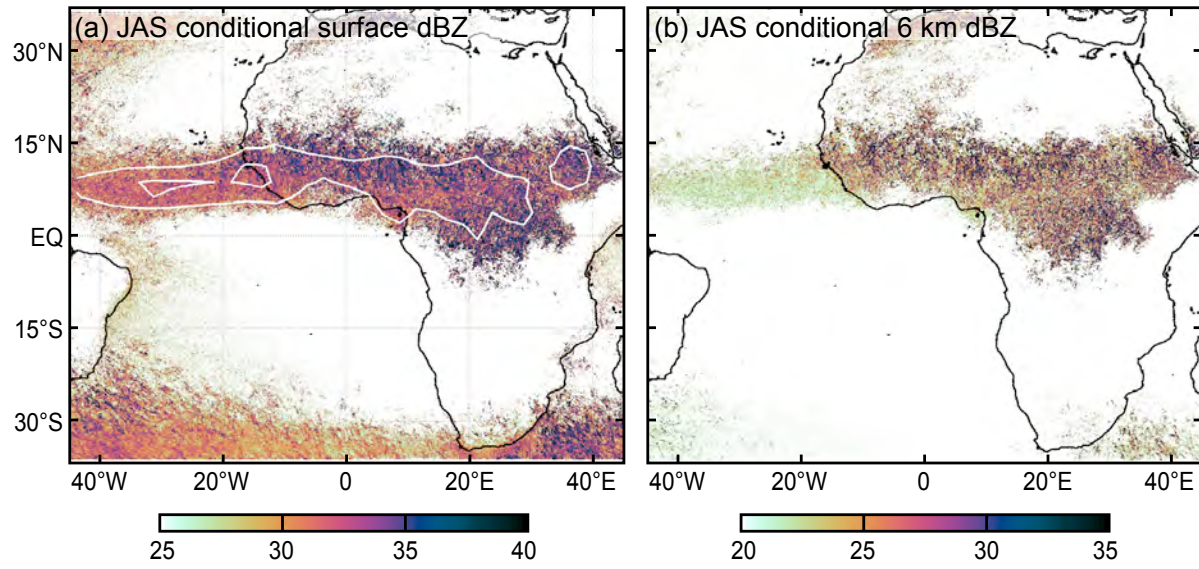


FIG. 4. JAS seasonal mean conditional reflectivity (dBZ) at surface (left) and at 6km (right) in the TRMM PR data (shaded) and rain rates in the GPCP dataset (left, white contours, the contour interval is 6mm/day, starting at 6mm/day).

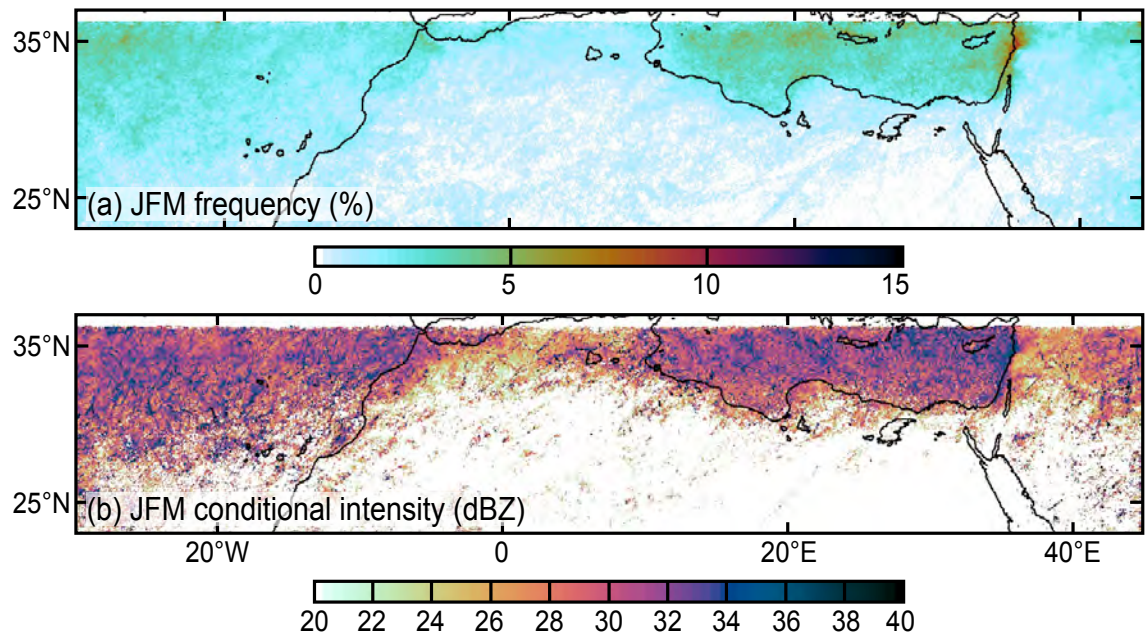


FIG. 5. Rain frequency (top) and intensity (bottom) in the southern Mediterranean sea and North African coast during JFM.

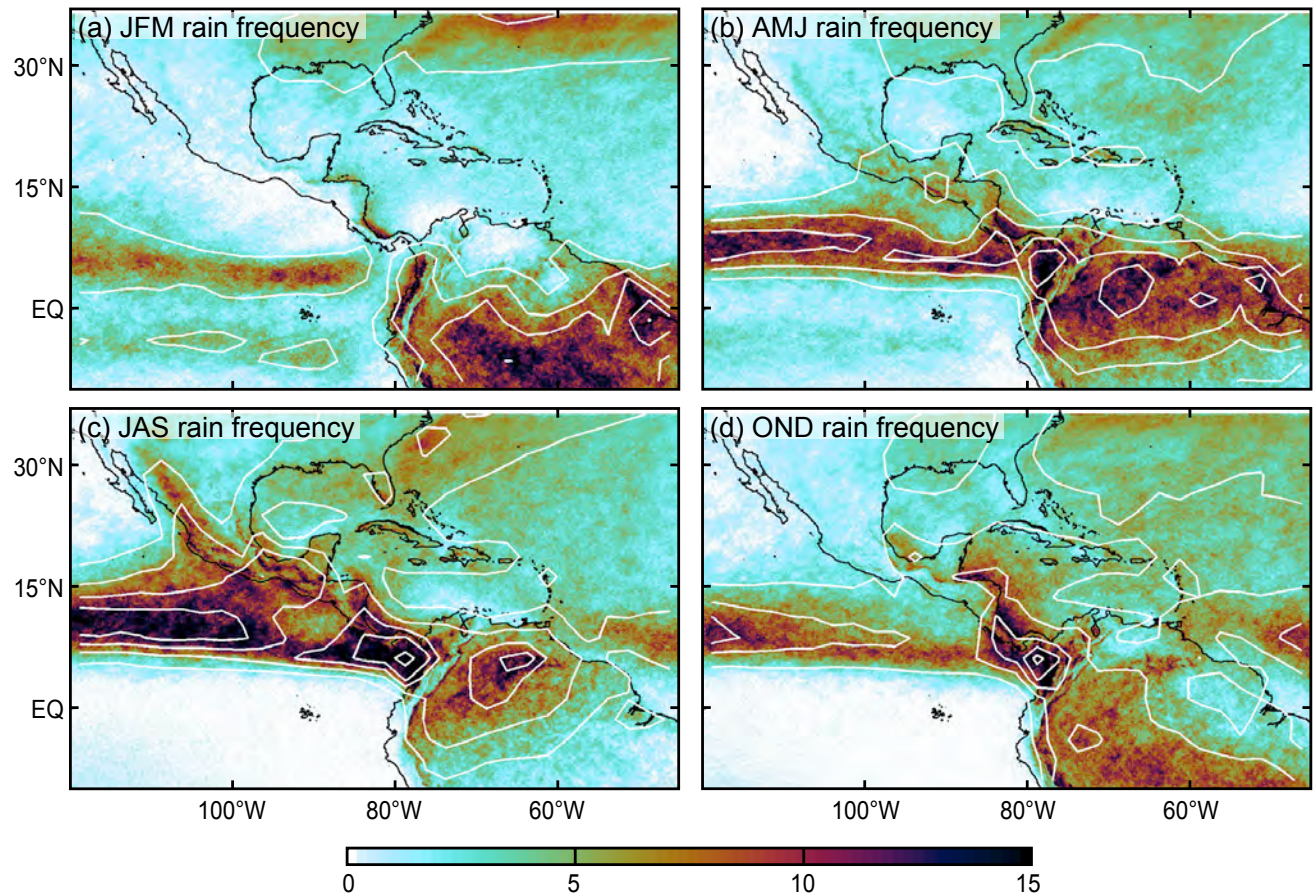


FIG. 6. Seasonal mean rain frequency in the TRMM PR data (shaded) and rain rates in the GPCP dataset (white contours, the contour interval is 3mm/day, starting at 3mm/day).

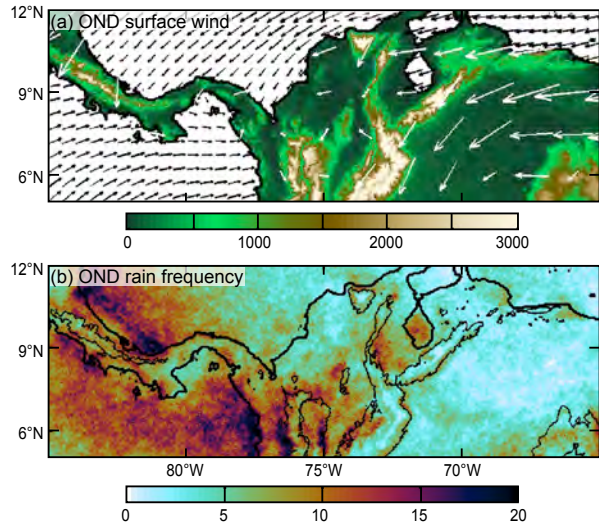


FIG. 7. (top) Topography and surface winds. Ocean surface winds are taken from Quicksat and are plotted in black every other gridpoint (i.e., at 1° resolution). Land winds are taken from the Interim ERA reanalysis and are plotted in white at 2.5° resolution. For clarity, wind over land is plotted with a scale 8 times as large as that used for ocean winds (that is, a wind vector will appear 8 times as large over land, for the same wind speed). (bottom) Rain frequency in the TRMM PR data. The light black contour indicates orography above 1000m.

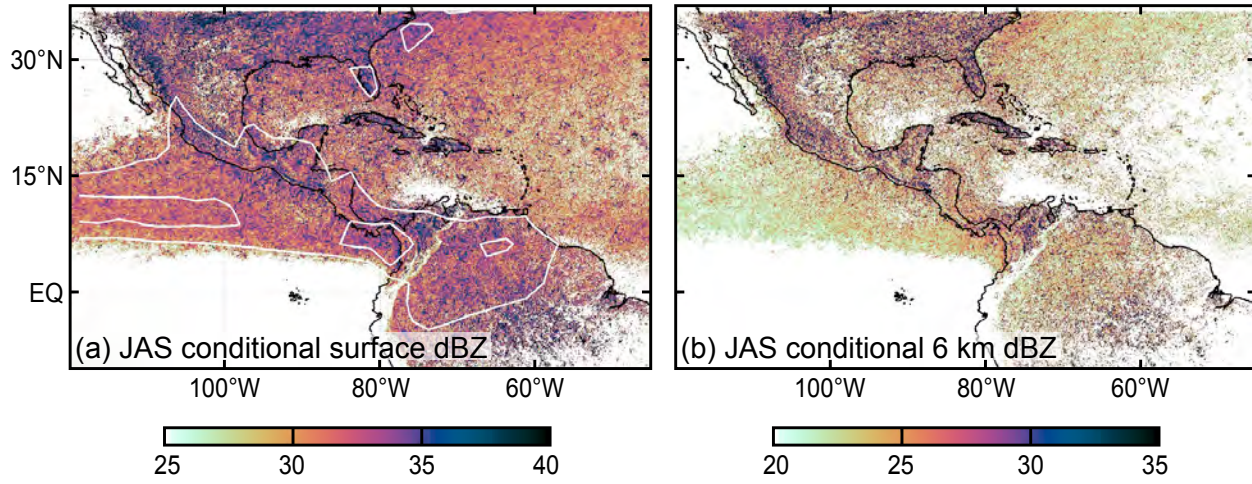


FIG. 8. JAS seasonal mean conditional reflectivity (dBZ) at surface (left) and at 6km (right) in the TRMM PR data (shaded) and rain rates in the GPCP dataset (left, white contours, the contour interval is 6mm/day, starting at 6mm/day).

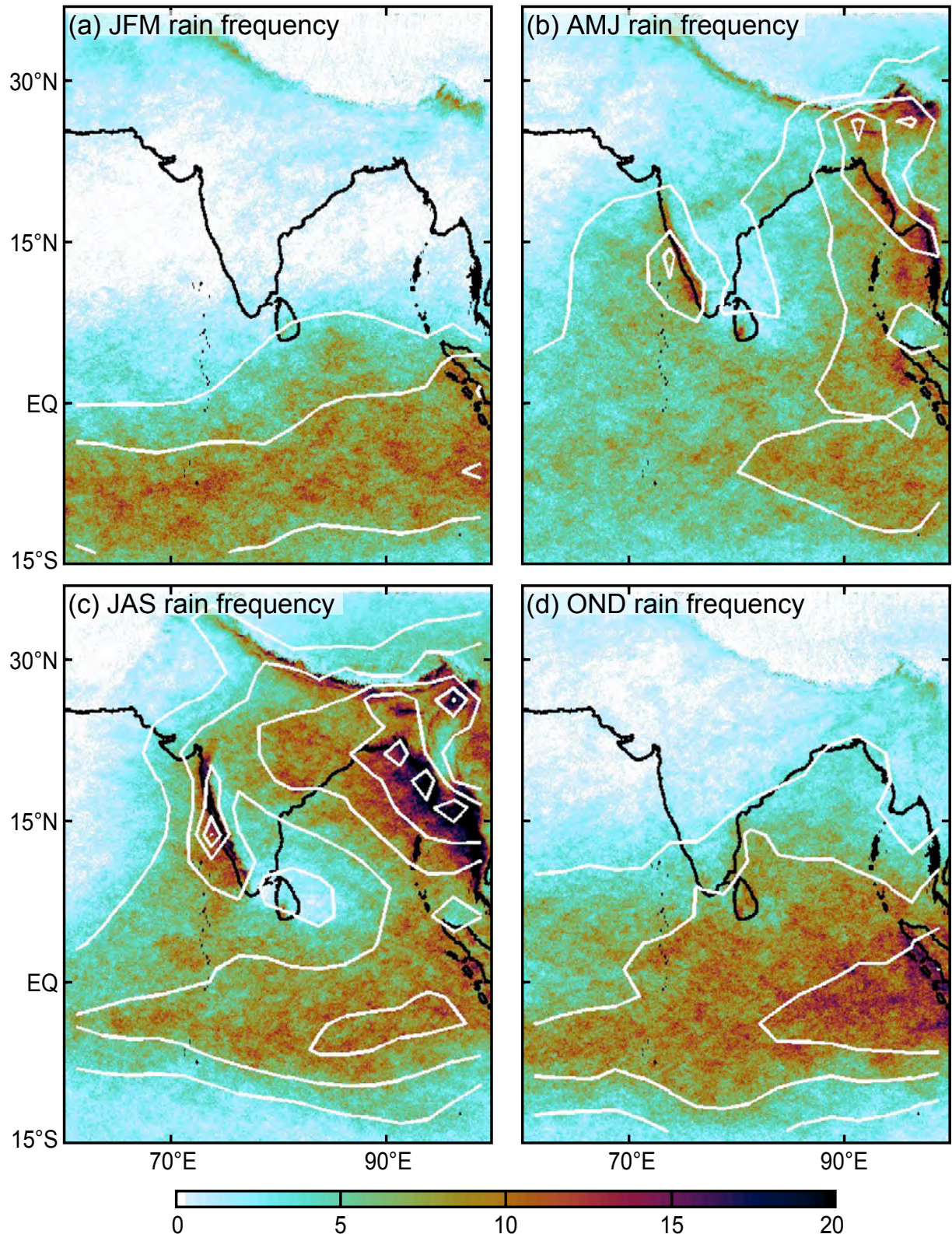


FIG. 9. Seasonal mean rain frequency in the TRMM PR data (shaded) and rain rates in the GPCP dataset (white contours, the contour interval is 3mm/day, starting at 3mm/day).

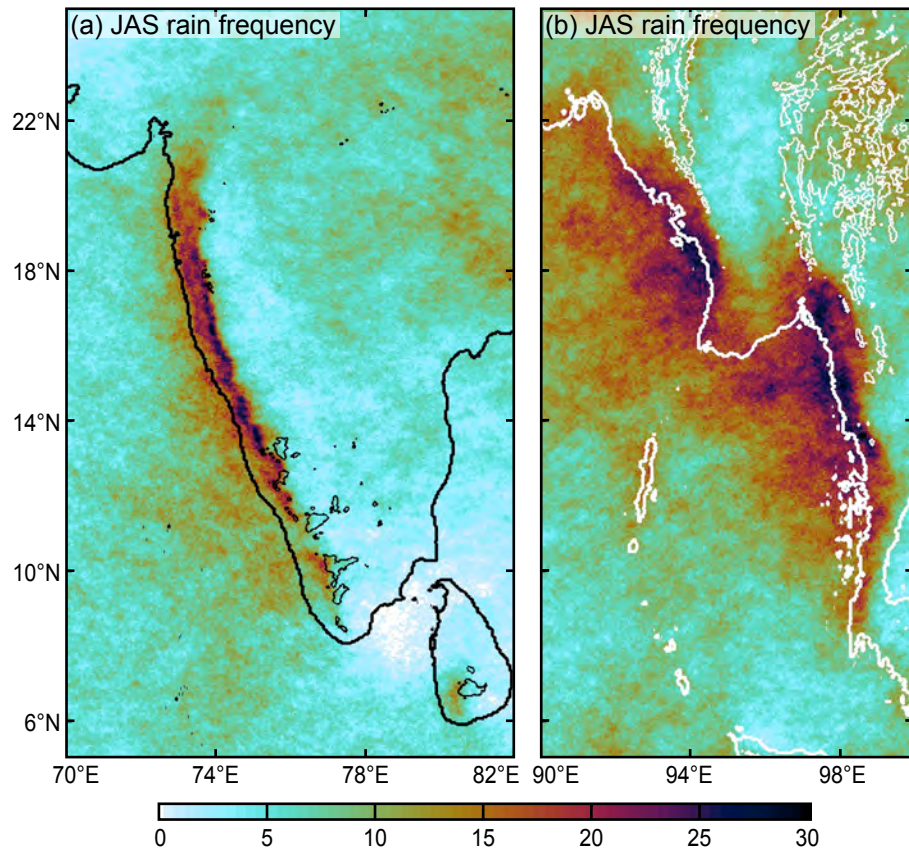


FIG. 10. Summertime rain frequency in the TRMM PR data along the (left) Ghats and the (right) Arakan mountains. The black (left) or white (right) contours indicate the coast and orography above 1000m.

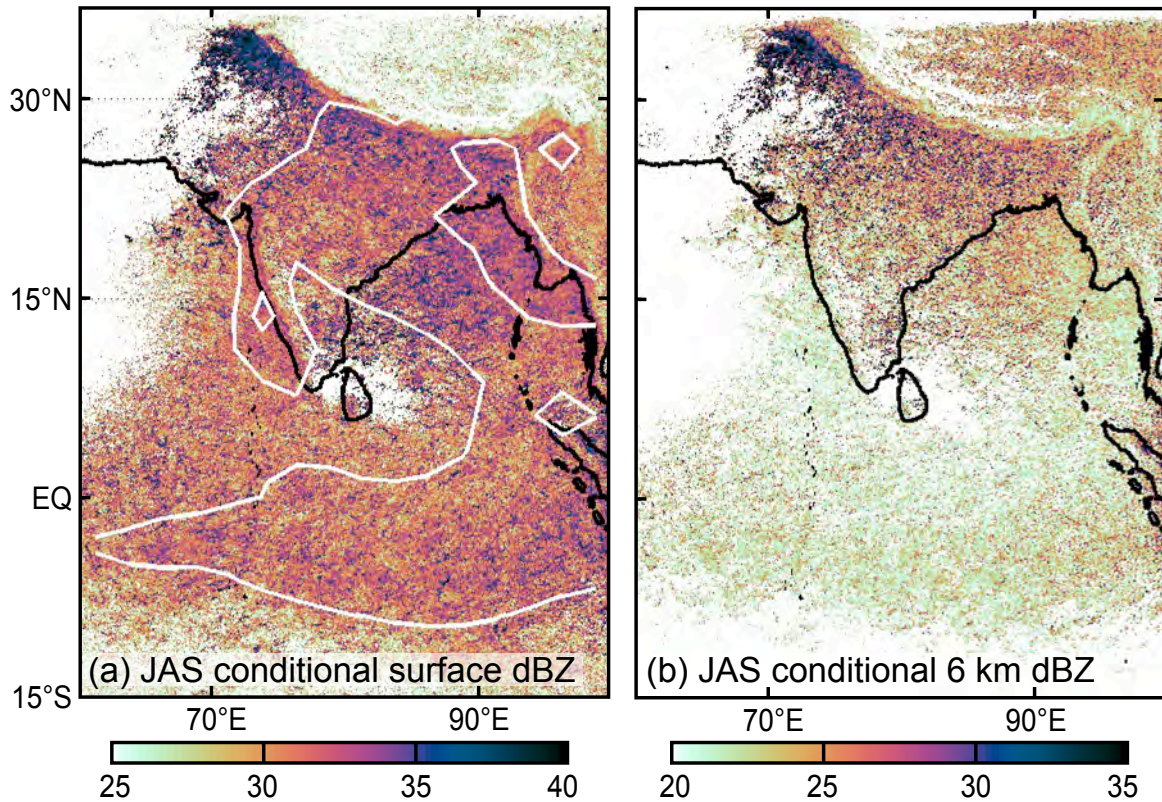


FIG. 11. JAS seasonal mean conditional reflectivity (dBZ) at surface (left) and at 6km (right) in the TRMM PR data (shaded) and rain rates in the GPCP dataset (left, white contours, the contour interval is 6mm/day, starting at 6mm/day).

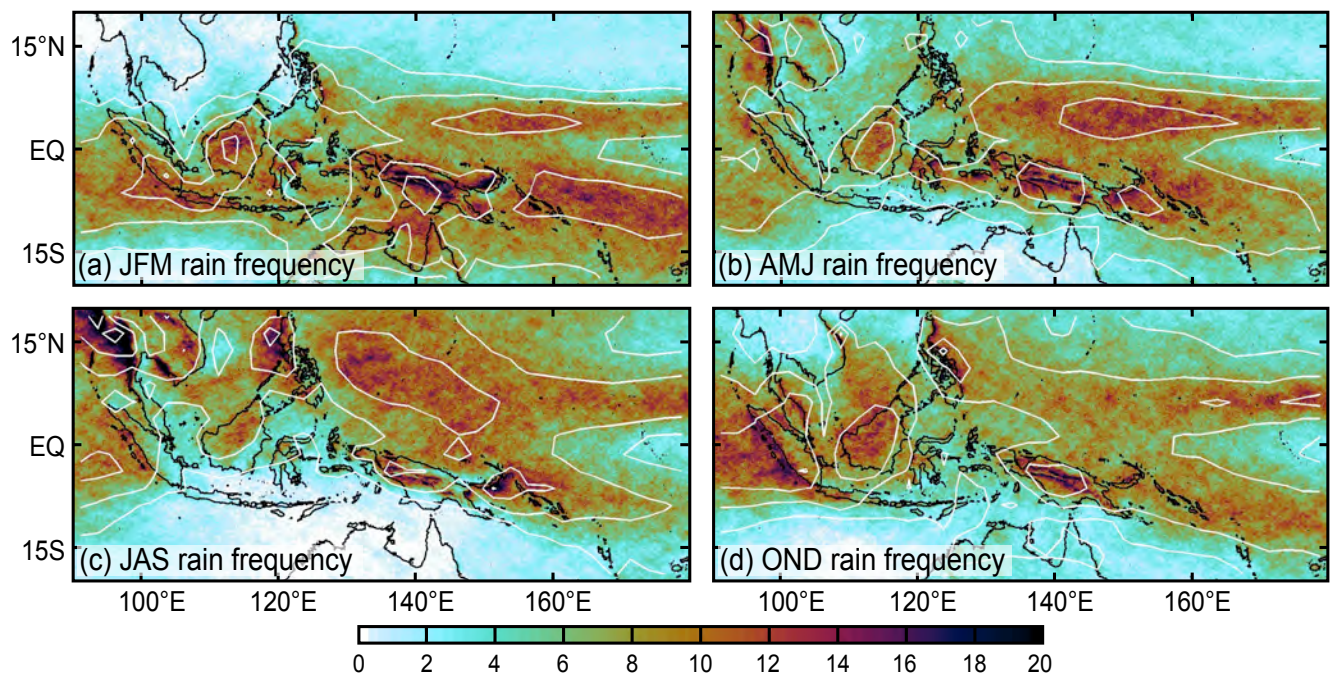


FIG. 12. Seasonal mean rain frequency in the TRMM PR data (shaded) and rain rates in the GPCP dataset (white contours, the contour interval is 3mm/day, starting at 3mm/day).

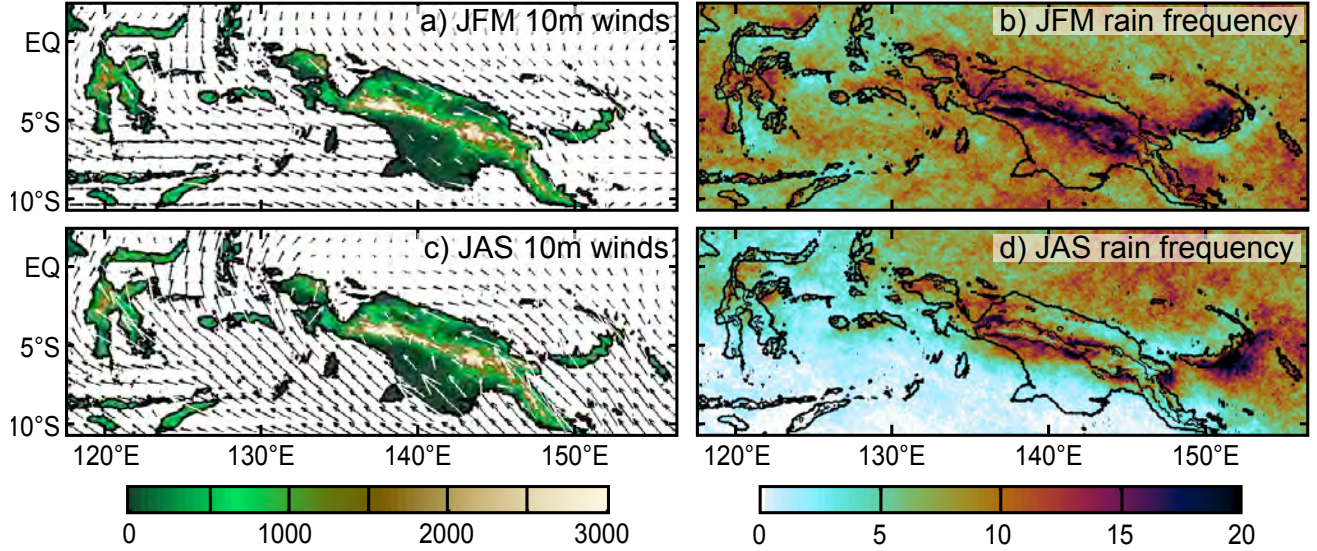


FIG. 13. (left) Topography and surface winds. Ocean surface winds are taken from Quikscat and are plotted in black every other gridpoint (i.e., at 1° resolution). Land winds are taken from the Interim ERA reanalysis and are plotted in white at 2.5° resolution. For clarity, wind over land is plotted with a scale 4 times as large as that used for ocean winds (that is, a wind vector will appear 4 times as large over land, for the same wind speed). (right) Rain frequency in the TRMM PR data. The light black contour indicates orography above 1000m.

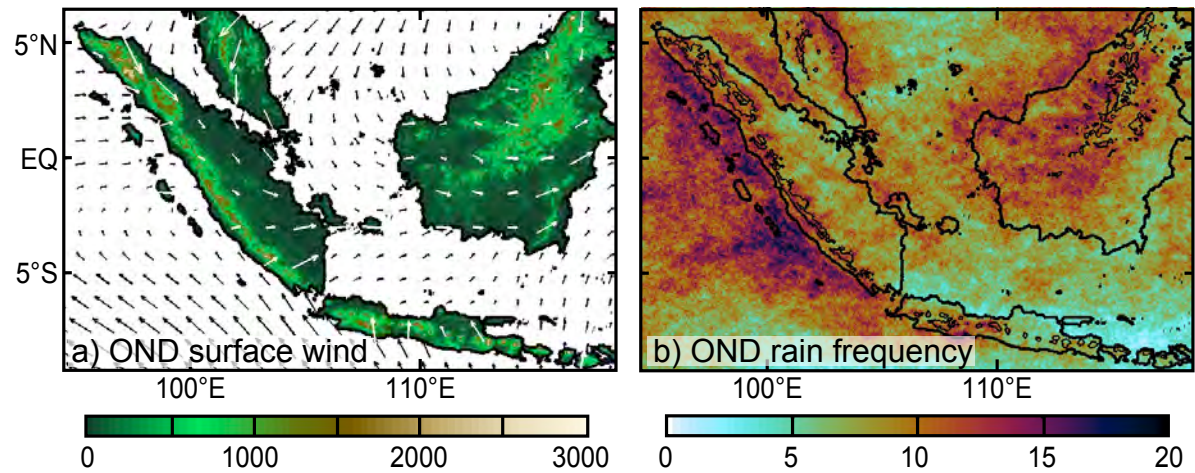


FIG. 14. As in fig.13.

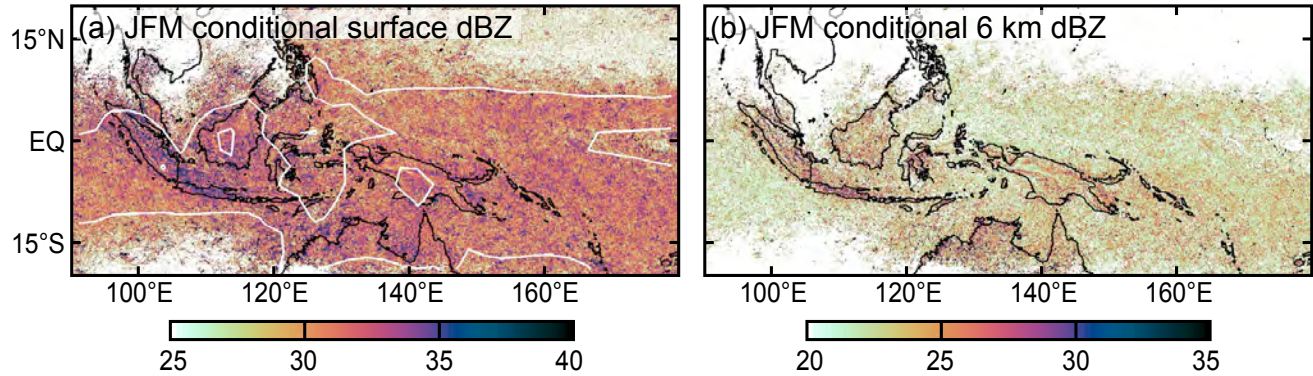


FIG. 15. JFM seasonal mean conditional reflectivity (dBZ) at surface (left) and at 6km (right) in the TRMM PR data (shaded) and rain rates in the GPCP dataset (left, white contours, the contour interval is 6mm/day, starting at 6mm/day).

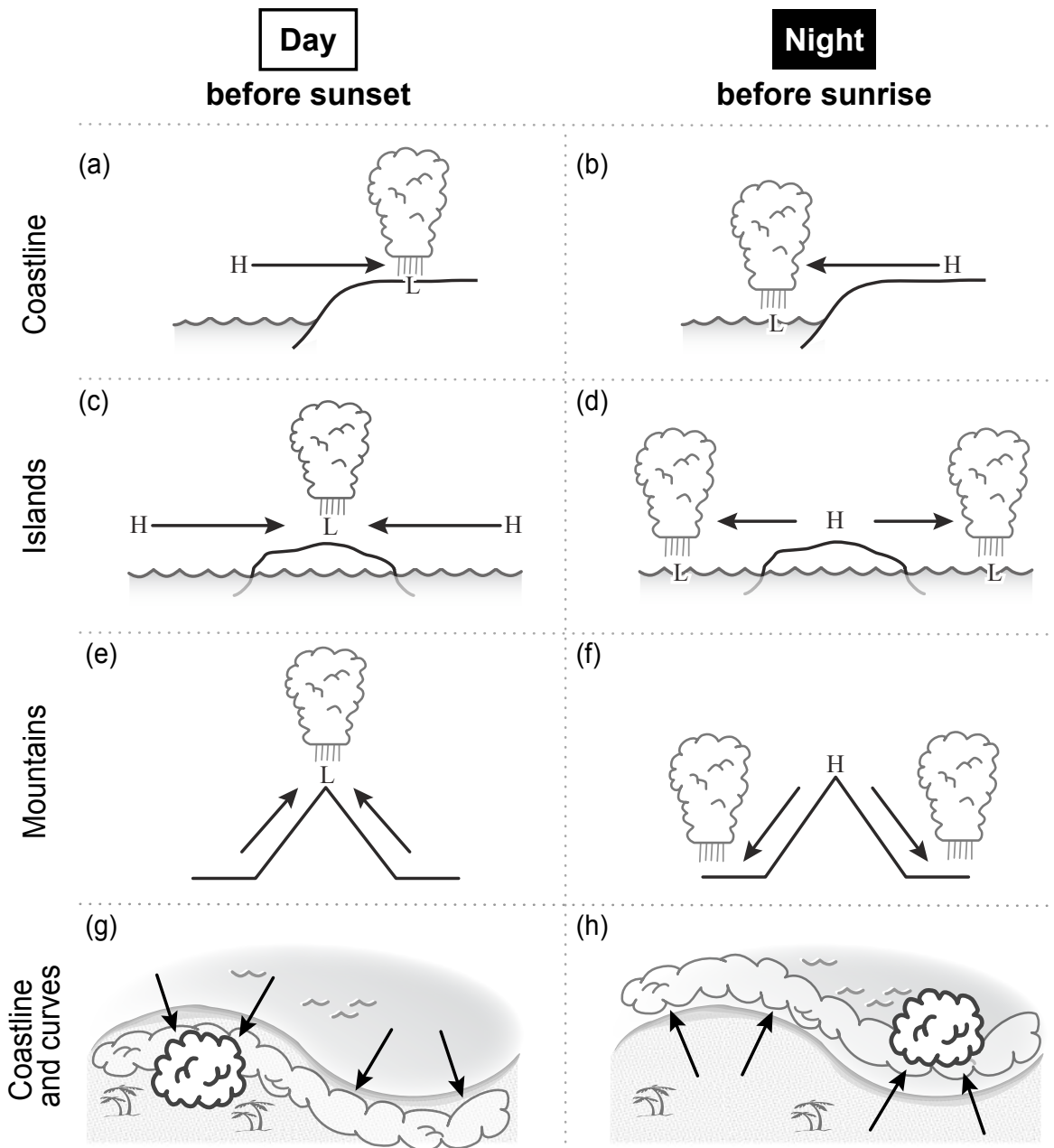


FIG. 16. Schematic explanation of the basic mechanism for sea breeze (top left and center) and land breeze (middle left and center) and for valley (top right) and mountain (middle right) breeze. The bottom panels depict the way in which bights and headlands influence land/sea breezes. Similar effects are a consequence of curves in the mountain ranges.

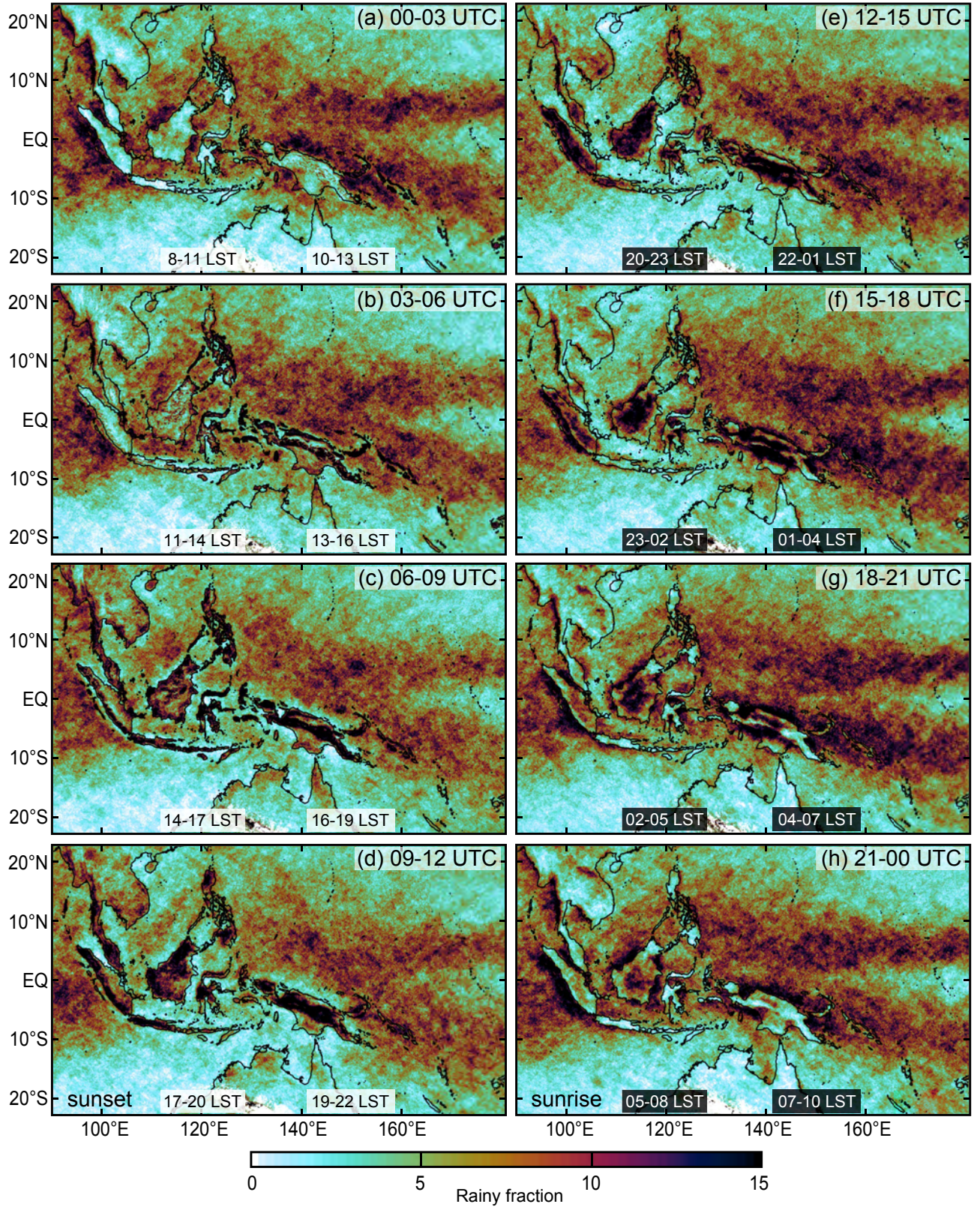


FIG. 17. Diurnal cycle of rainfall frequency in 3-hourly increments for the West Pacific region. The left panels are for daytime, the right panels are for nighttime.

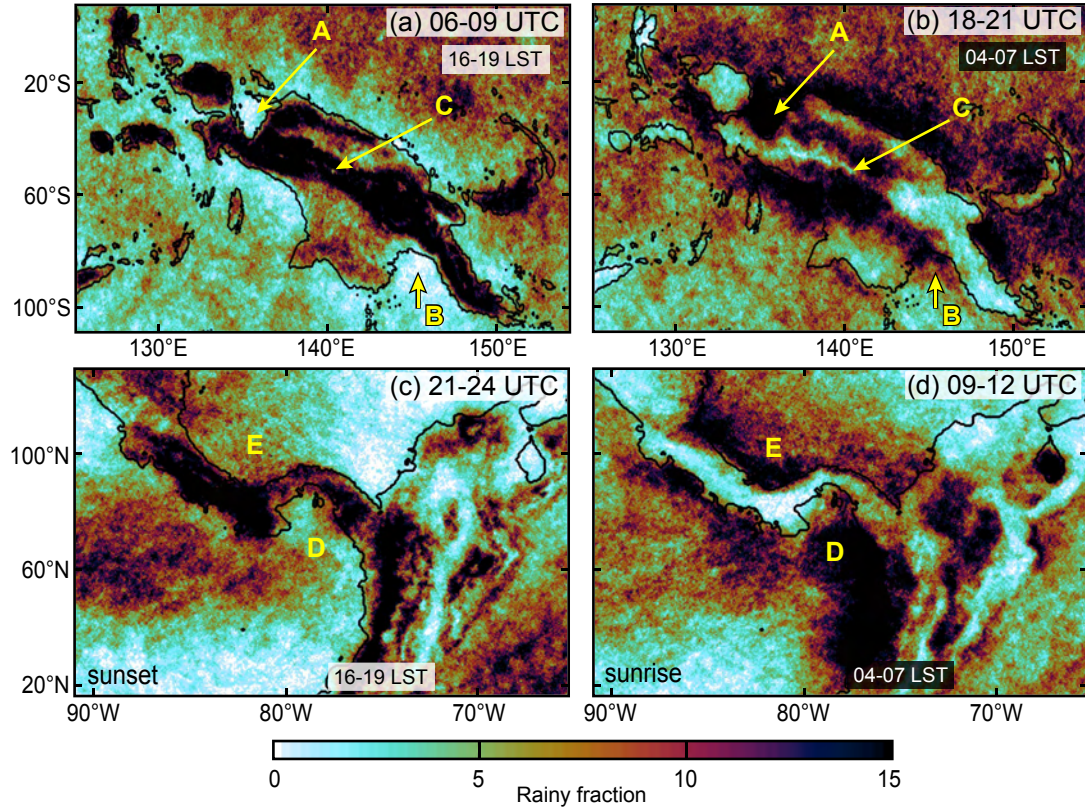


FIG. 18. Late afternoon (left) and pre-dawn (right) rainfall frequency over New Guinea Island (top) and the Panama Isthmus (bottom).

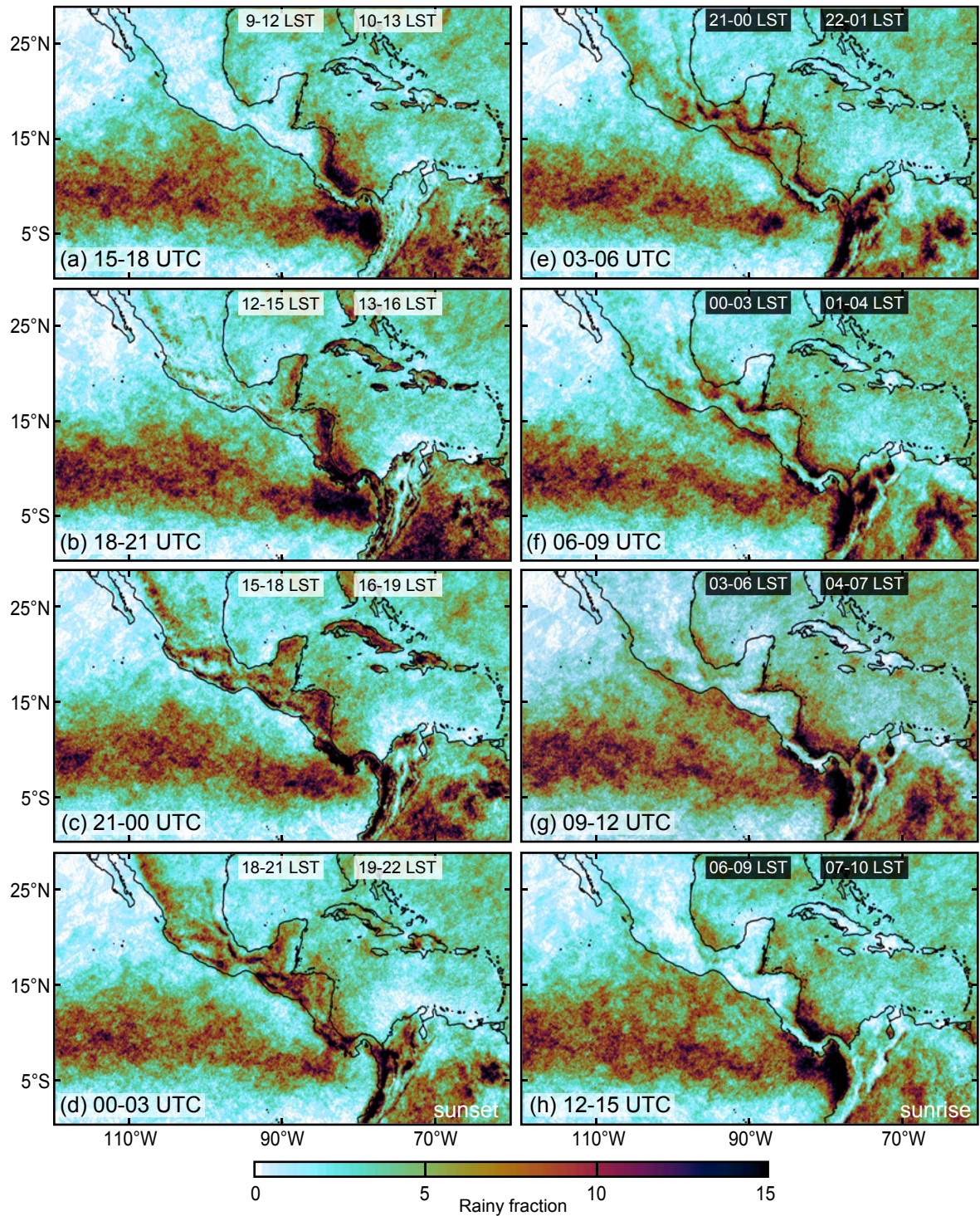


FIG. 19. Diurnal cycle of rainfall frequency in 3-hourly increments for the Middle America region. The left panels are for daytime, the right panels are for nighttime.

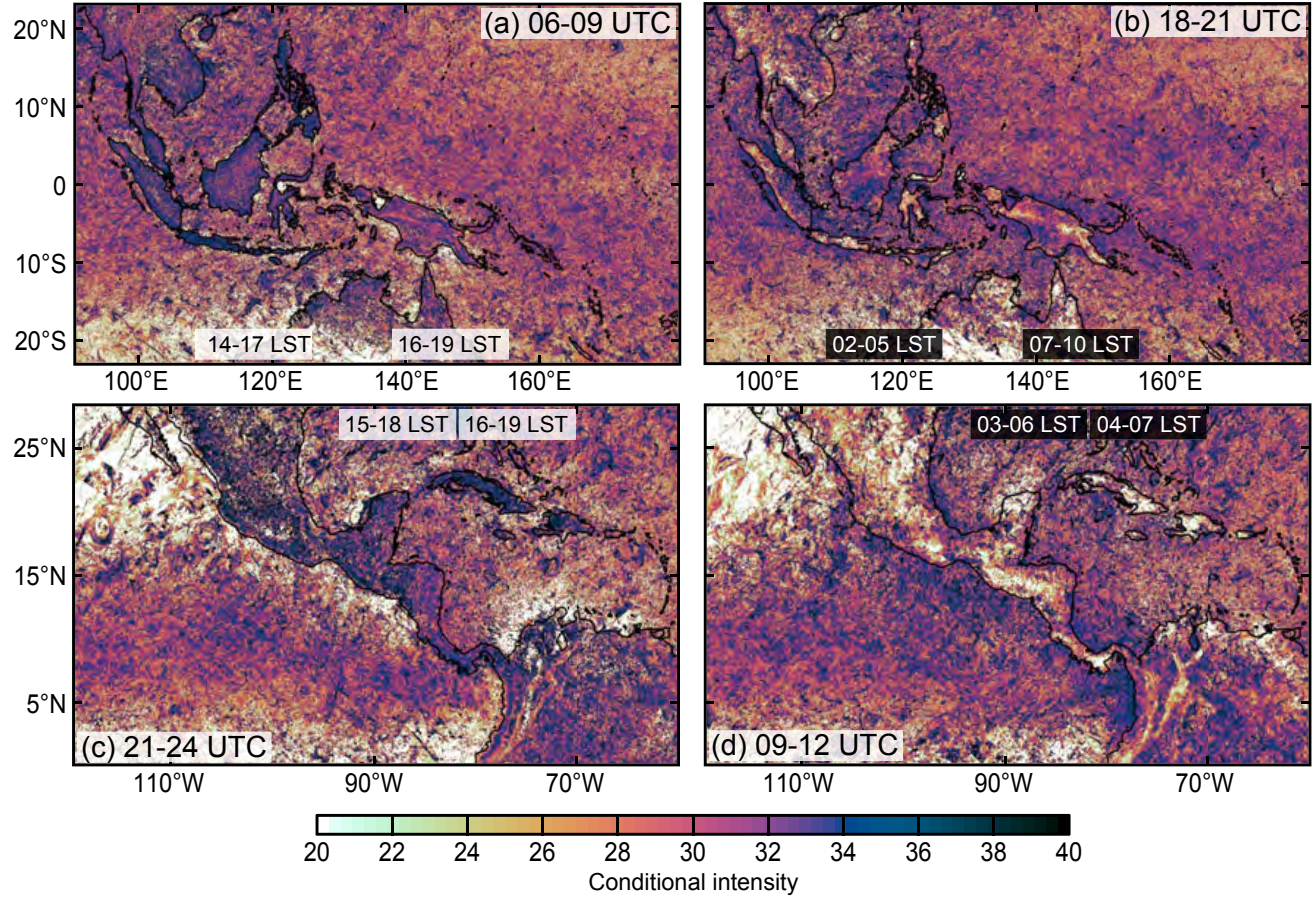


FIG. 20. Conditional rainfall intensities for hours near sunset (left) and near dawn (right) for the West Pacific (top) and the Middle America (bottom) regions.